1.1 The Photon Veto Detectors

1.1.1 Physics Requirements for Photon Veto System

Photon vetoes are required to suppress the dominant background originating from the decay $K^+ \to \pi^+\pi^0$ (BR=20.7%) to the specified level. The average inefficiency for the rejection of the π^0 should be smaller than 10^{-8}. The photon vetoes need to have hermetic geometrical coverage up to 50 mr for the photons originating from the kaon decays occurring in the decay region (from 5 to 65m after the final collimator). With such a configuration, only about 0.2 % of the $K^+ \to \pi^+\pi^0$ events have one photon from the π^0 left undetected.

The geometry of the experiment suggests partitioning of the detector into three different angular regions, each instrumented by three different detector technologies:

- Large Angle Vetoes (LAV), covering the angular region between 8.5 mr and 50 mr, distributed along the decay volume and spaced by 6m in the upstream region and by 12m downstream, according to the layout in Figure 1.
- The NA48 Liquid krypton calorimeter (LKR), covering angles between 1 and 8.5 mr (see section 1.1.4 on page 47)
- Small angle vetoes covering the region down to zero degrees (SAC) and the zone around the inner radius of the LKR (IRC) calorimeter. These will have suitable overlap in the angular acceptance to cover the beam pipe and an inner radius smaller than that of the beam pipe (see section 1.1.5 on page 50).

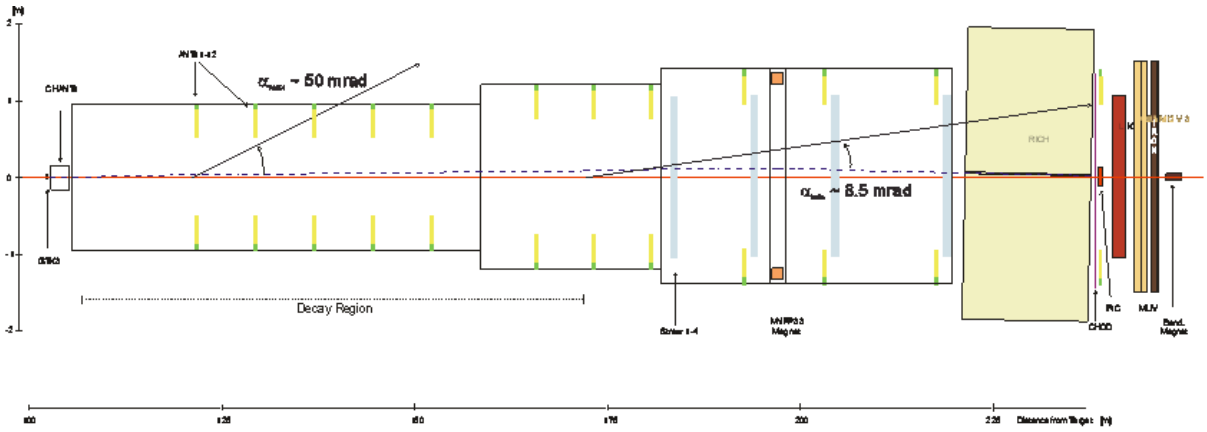

Figure 1 Longitudinal View of the LAV detector (yellow).

The kinematics of $K^+ \to \pi^+\pi^0$ decay in the NA62 decay volume are such that, with a cut on the momentum of the charged pion, only three possible configurations are present:

- both photons from the π^0 hitting the forward calorimeters with a total energy larger than 20 GeV;
- one photon in the forward calorimeters and the other one in the Large Angle Vetoes;
- one photon in the forward calorimeters and the other one lost at angles larger than 50 mr.

This last combination occurs only in 0.2 % of the decays. In order to achieve the required π^0 rejection, all photon veto detectors must have an inefficiency lower than 10^{-4}. With this requirement, the major contribution to the global inefficiency comes from the 0.2 % of events where only one photon is detected.

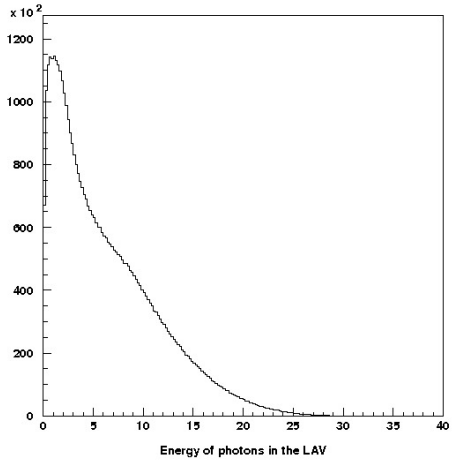

Figure 2 Photon energy distribution in the LAV.

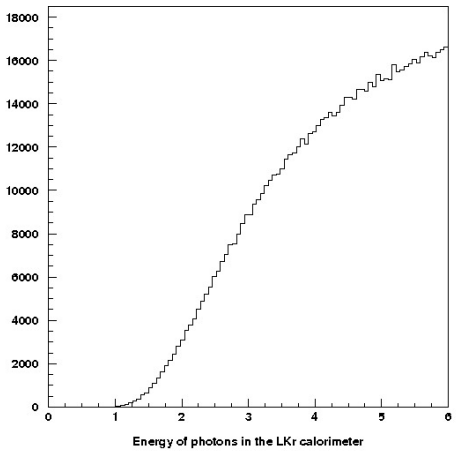

Figure 4 Minimum photon energy in the LKR.

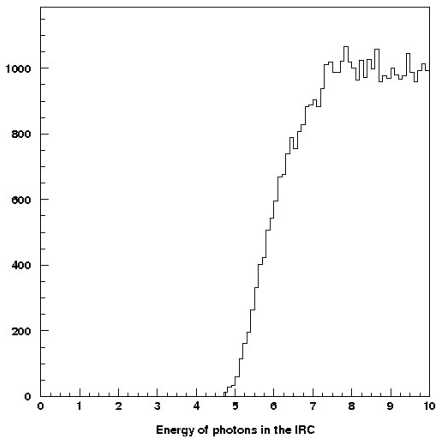

Figure 3 Minimum photon energy in the IRC

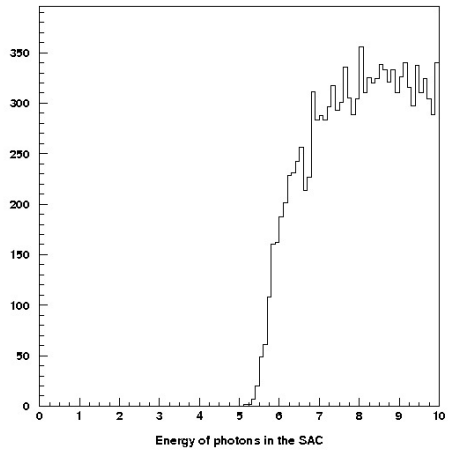

Figure 5 Minimum photon energy in the SAC

A simulation of the decay kinematics and of the geometrical acceptance has been made to compute the average photon detection inefficiency. It was done using an estimation of the inefficiency of each detector based on experimental measurements from test beams and with the NA48 detector. The average π^0 inefficiency is computed weighting each photon with the inefficiency of the hit detector at the photon energy.

The results shown refer to 10^7 $K^+ \rightarrow \pi^+\pi^0$ decays generated with a cut on the charged pion momentum between 15 and 35 GeV. The photon energy in the Large Angle Vetoes is distributed between below 10 MeV and 30 GeV (Figure 2). The minimum photon energy in the LKR calorimeter is 1 GeV (Figure 4), while in the IRC and SAC it is around GeV (Figure 3 and Figure 5).

The average π^0 inefficiency is reported in Table 1, with and without imposing a cut on the π^+ momentum between 15 and 35 GeV. The fraction of events which mainly contributes to the average inefficiency is also shown in Table 1, imposing the cut on the π^+ momentum. This fraction is defined as the ratio between the number of the events contributing to the inefficiency and the total number of the accepted events (in this example 2747513).

Table 1 Fraction of inefficient events

Destination of the two photons	Number of events contributing to the inefficiency	Fraction (%)
Both photons undetected	0	0.00
One photon undetected, the other in the LAV	0	0.00
One photon undetected, the other in LKR,IRC,SAC	5312	0.19
One photon in the LAV, the other in LKR,IRC,SAC	510534	18.58
Both photons in LKR, IRC, SAC	2231667	81.22
Average inefficiency without π^+ momentum cut	$8.4*10^{-8}$	
Average inefficiency with π^+ momentum cut	$1.6*10^{-8}$	

An in-depth look at inefficient events shows that they are characterized by one low energy photon that is either outside the acceptance of the LAV or inside it, but with very low energy and high inefficiency. The other photon is mainly hitting the LKR calorimeter, with an energy larger than 35 GeV, or the first IRC, with an energy larger than 60 GeV. It is then mandatory to have an inefficiency of the LKR lower than 10^{-5} at those energies to reduce the contribution from these events to the average π^0 rejection inefficiency.

1.1.2 Photon-Veto detector Efficiency Studies

For the large-angle photon veto detectors, a comprehensive research and development program was carried out in Frascati in 2007 in order to guide the choice of technologies to be used. Three possible technologies for the LAV system were considered. The first design, originally proposed for use in the (now cancelled) CKM experiment at Fermilab, featured a modular structure consisting of alternate layers of 1-mm thick lead plates and 5-mm thick scintillating tiles, readout by wavelength-shifting fibers. A second option, adopted for the construction of the electromagnetic calorimeter for the KLOE experiment, featured a structure consisting of 1-mm diameter scintillating fibers embedded between 0.5-mm thick lead foils. The third solution made use of lead-glass crystals obtained from the dismantled electromagnetic calorimeter of the OPAL experiment (1). Prototype detectors based on each of the three technologies have been obtained or constructed. Experimental tests conducted with the electron beam at the Frascati BTF demonstrated that all three technologies are suitable for use in the experiment (2). The results obtained for the inefficiency are summarized

in Figure 6. The efficiency for detection of low-energy electrons is similar for all three technologies. For these initial tests at the BTF, the results for the lead-glass solution were obtained with a stack of four OPAL modules. Since there is a significant practical advantage to adapting existing hardware for the NA62 LAV system, the performance of the OPAL modules was further investigated. In early 2008, a 25-block staggered array of lead glass crystals was tested at the Frascati BTF. In particular, the efficiency of a lead-glass array for the detection of 470-MeV electrons was studied as a function of the impact position. These studies essentially confirmed the findings presented in Figure 6 (3). We therefore decided to base the LAV design on the OPAL detectors, as described in the following sections.

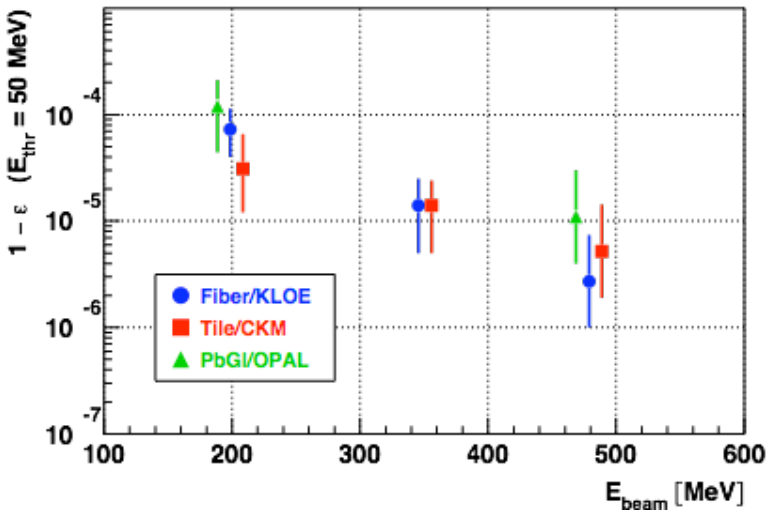

Figure 6 Measured efficiencies vs energy for three types of photon veto detector.

Dedicated studies of the photon detection efficiency of the NA48 LKR calorimeter were performed using two data samples from the experiment (4), as noted below.

In 2004, $K \rightarrow \pi\pi^0$ decay events were collected during a dedicated run with the NA48 apparatus, using as trigger criteria a drift chamber multiplicity and hodoscope signal requirement to select single track events, as well as a muon veto. $K \rightarrow \pi\pi^0$ decays were identified offline using missing mass cuts. Various other cuts were made to eliminate backgrounds. Among the clusters not associated with the track, the one with the least energy was assumed to be the lower energy photon from the π^0 and used to tag the other photon. Among 730k events, the other photon was not detected in five cases. Allowing for uncertainties in the background rate and other systematics, the inefficiency of the LKR for the detection of photons with $E > 10$ GeV was found to be less than 9×10^{-6} at 90% CL.

An alternative measurement of the LKR calorimeter efficiency was performed during a dedicated run in 2006. In this run, a 25-GeV/c secondary electron beam was produced using protons from the SPS, and traversed the NA48 apparatus, producing bremsstrahlung photons. For events in which the photon was emitted from an interaction with the 1.3% X_0 of material upstream of the spectrometer magnet, the initial beam direction defined the impact point of the photon on the calorimeter, while the beam itself was deflected horizontally by the magnet, so that it arrived at the calorimeter with a

displacement of about 12 cm from the impact point of the photon. The detection efficiency measured for photons with E > 10 GeV was consistent with the result of the 2004 study using $K \to \pi\pi^0$ decays.

The baseline design calls for the small-angle calorimeters to be constructed with shashlyk technology. During the 2006 test run, a prototype shashlyk SAC module was constructed and tested using the 25-GeV electron beam (4). The active part of the detector was assembled from layers of 20.5 × 20.5 cm^2, 1.5-mm thick lead plates and 1.5-mm thick scintillator plates, for a total of 16 radiation lengths. The light was read out with wavelength shifting fibers coupled to four photomultiplier tubes. During the tests the detector was placed between the two planes of the NA48 scintillator hodoscope, which helped define the trigger. The electron beam was deflected to point at the SAC module; the beam position was varied to collect information on the variation of response as a function of impact position. The offline selection also required a full-momentum track in the NA48 spectrometer. Of 36k total tracks passing the offline cuts, none were found without an associated signal in the SAC prototype. The corresponding upper limit on the inefficiency for 25-GeV electrons is 6.4×10^{-5} at 90% CL. A refined analysis with the whole statistics gave a value for the inefficiency of $(2.9\pm0.3)x10^{-5}$.

The results from these tests have been used to compute the average inefficiency as described in 1.1.1.

1.1.3 The Large Angle Detectors (LAV)

1.1.3.1 General Layout of the LAV

The Large Angle Veto is to be composed of 12 stations situated between 120 and 240 m along Z (Figure 1). The first eleven stations are part of the vacuum decay tube, while the last one is located outside the vacuum tank.

The basic building blocks of these detectors are lead glass crystals with attached photomultipliers (PMT) from the former OPAL electromagnetic calorimeter (see 1.1.3.2). Four crystal detectors (lead glass crystals + PMTs) are mounted on a common support structure forming an azimuth segment. Inside the vacuum tube the azimuth segments are assembled to form a complete ring of lead glass blocks. Each LAV stations is made up of 4 or 5 rings, which are staggered in azimuth providing complete hermeticity of at least three blocks in the longitudinal direction. All the counters in a complete ring of lead glass lie in one plane that is perpendicular to the beam line, with all the PMTs on the outside of the ring.

1.1.3.2 The Basic Crystal Detectors

1.1.3.2.1 Mechanical Assembly of the Crystals

Each lead glass block from the former OPAL experiment has the shape of a truncated prism of Schott SF57 lead glass (1), whose properties are shown in Table 2. The blocks are available with different shapes and dimensions (with minimal variations between different types). Figure 8 and Table 3 describe these differences and all dimensions which are relevant for the design of the modules. The block length (BL in the figure) is always 370 mm. One of the (almost) square faces of the lead glass has a 1 cm-thick steel flange glued to it (Figure 7). This flange has four threaded holes for fixing the counter to the support bracket, one for the connection of a calibration optical fibre, and a central large hole for the passage of a cylindrical light guide for light collection. The light guide is a cylinder of SF57 lead glass with a diameter of 73 mm and a height of 60 mm. It is glued to the lead glass block and, at the other end, to a Hamamatsu R2238 photomultiplier. An external mu-metal shield, enclosing the guide and the PM, is glued to the steel flange.

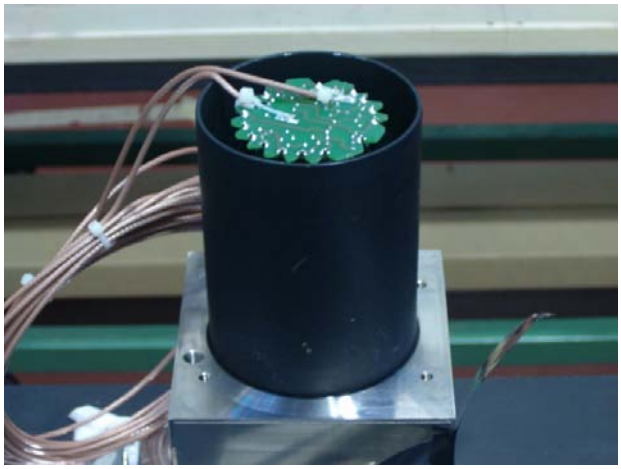

Figure 7 The steel flange

Table 2 Physical characteristics of the SF57 lead glass

Density	5.51 g/cm^3
Radiation length	1.54 cm - 8.49 g/cm^2
Moliere radius	2.61 cm
Interaction length	20.6 cm - 115 g/cm^2

1.1.3.2.2 Photon Detector Assembly

The photomultiplier pins are directly soldered to the standard Hamamatsu divider for the R2238 tube mounted on a round printed circuit board. HV and signal cables are made of Teflon insulated RG316 cable, with a length varying from 4.5 to 6.2 m (depending on the ring to be built). The HV ground connection on the divider is decoupled from the signal ground by a 10 Kohm resistor in series. On the side opposite to the PMT, the signal cable has a mini coax connector (SOURIAU type RMDXK10D28), while the HV cable has a Burndy pin (type RM24M-9K) on the voltage wire and a faston connection on the ground.

Block type	W2 (mm)	mumetal length (mm)
15	95.461	110
14	95.598	110
13	95.808	110
12	96.086	110

11	96.426	110
10	96.820	115
9	97.261	125
8	97.740	145
7	98.250	145

Table 3 Types and dimensions of the blocks

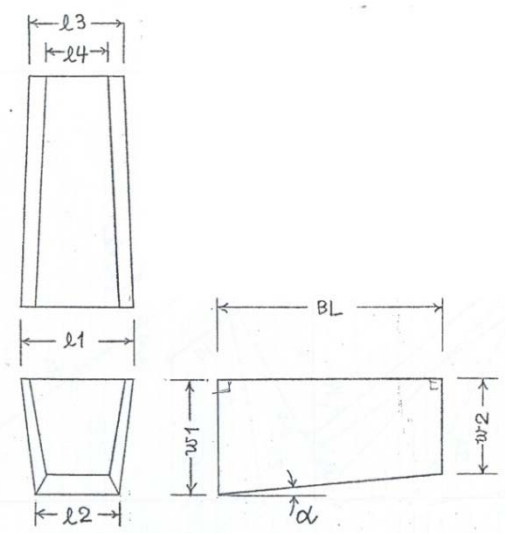

Figure 8 Shape and dimensions of the block

1.1.3.2.3 Validation and Selection of Existing Crystal Detectors

The final number of available OPAL lead-glass blocks after the validation test (see 1.1.3.3) is expected to be close to the quantity of blocks (2496) required for NA62. A possible optimisation of the assignment of blocks to the different rings is at the moment under study. Table 4 lists the provisional assignments of block types to each detector station.

Table 4 Provisional assignments of block types to the detector modules and layers.

Module	Number of Layers	Crystals/layer	Block types used
LAV 1	5	32	15
LAV 2	5	32	14
LAV 3	5	32	4*11 + 1*14
LAV 4	5	32	4*13 + 1*14
LAV 5	5	32	15
LAV 6	5	48	13
LAV 7	5	48	14
LAV 8	5	48	2*11 + 3*15
LAV 9	4	60	12
LAV 10	4	60	10
LAV 11	4	60	9
LAV 12	4	64	2*7+2*8

1.1.3.3 Testing and Characterization of the Crystal Detector Blocks

Before re-using the OPAL crystal detectors , a number of tests are performed to validate each crystal detector block :

- Operational checks of the PMT (HV, signal, and light tightness)
- A measurement of the PMT amplification (gain) as function of anode voltage
- A measurement of the photoelectron yield in the crystal with the connected PMT

1.1.3.3.1 The Lead Glass Test Station

The gain and the photoelectron yield of all the PMTs will be measured in conjunction with their lead-glass crystals using the Lead Glass Test Station (LGTS). The LGTS (see Figure 9) consists of a light-tight box that can accommodate twenty lead glass detectors (LG), twelve for testing and eight for triggering on cosmic ray particles. A bundle of 12 (+2 spares) optical fibres distributes light pulses from a LED. The whole system is remotely controlled by a personal computer and signals are acquired by a VME ADC module (CAEN V792, 12 bit 0-400 pC).

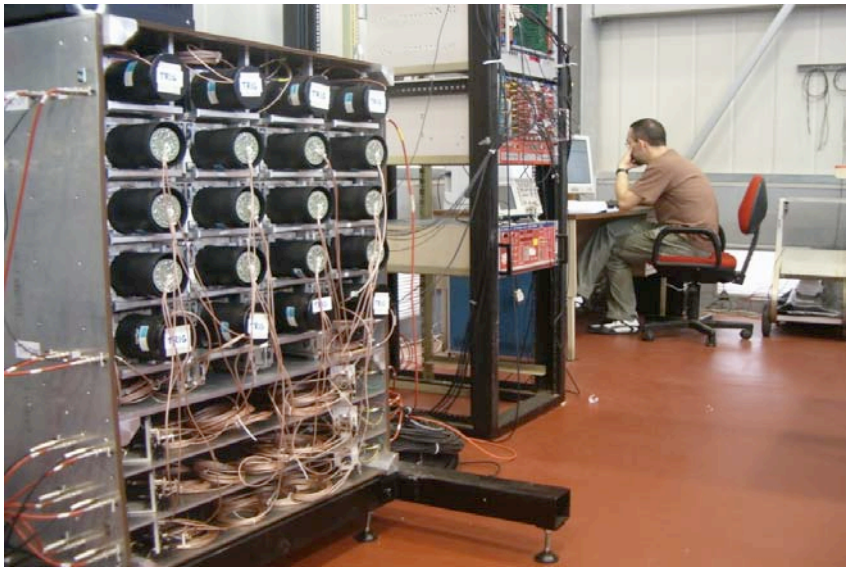

Figure 9 The Lead Glass Test Station.

Optical fibres can inject light pulses using a small inspection window present in the wrapping. The external lateral sides house the High Voltage (HV) and signal connectors. An LED system has been designed for the LGTS to distribute the light generated by one LED to all 12 blocks under test. The temperature of the LED is stabilized at a level of about 0.1 °C by means of a Peltier cell. The amplitude of the light pulses can be varied by more than a factor of 10 and is software controlled via an RS-232 interface. Pulses can be triggered either by an internal clock or by an external source, the typical trigger rate is 100 Hz. The LGTS is used to measure the gain curve of each PMT and to

equalize the responses. Beforehand, checks are made to see that the block can stand high voltage without discharging and that the current from the PMT, at a fixed HV value, is within specifications.

1.1.3.3.2 Gain Measurement

The gain G of a PMT can be measured using several light pulses having the same amplitude. If R is the measured response, then the mean value <R> and the standard deviation σ_R are related to the gain by the relation:

$$\sigma_R^2 = \langle R \rangle \cdot G \cdot \left(1 + \delta_{SER}^2\right) \qquad (1)$$

where δ_{SER} is the single electron response (SER) fluctuation contribution. This term depends on the gain value and the PMT structure, and can be non negligible, of order 20-30%. A good approximation of its value is obtained by the relation:

$$\delta_{SER} = G^{-1/N} \cdot \left[\frac{\left(\prod k_i\right)^{1/N}}{k_1} \right]^{\alpha}$$

where

N is the number of dynodes

$k_1 ... k_N$ is the fraction of the HV applied to the i-th dynode

α is a parameter usually comprised between 0.6 and 0.7, which is kept here at 0.6.

After fixing a HV value, <R> and σ_R are measured for a sample of typically 10^4 light pulses generated with the same amplitude over a relatively short time period (100 s) . Then the measurement is repeated for a different value of the light pulse amplitude. G is extracted by applying the obtained data with a least square fit to equation (1).

The whole procedure is then repeated varying the HV between 1150 V and 1350 V (in 50 V steps). The gain curve G(V) obtained in this way is then obtained by analytical interpolation of the measured points.

1.1.3.3.3 Photo-electron yield

The photoelectron yield (PeY) for each block is defined as the number of photoelectrons released by the detector per MeV deposited by a MIP. It depends mainly on the photocathode quantum efficiency, on the photon collection efficiency (crystal to PMT) and on the photon yield of the crystal. Since the crystal and the PMT are glued together, this number is the main figure of merit for a detector block. At the beginning of 2008 the PeY was measured for 40 randomly chosen detector blocks. Using a tracker it was possible to determine the detector response as a function of distance from the photocathode of a straight MIP crossing the crystal, and it was shown to be flat.

The total charge measured when a MIP crosses the detector is :

$$Q = G \cdot N_{pe} = G \cdot E \cdot PeY$$

where G is the PMT gain and E is the energy released by the MIP. One can evaluate for each block the PeY from the measured response Q when a cosmic ray crosses the detector and the known gain G given by the gain curve G(V). The average energy E released by a MIP impinging orthogonally on the crystal is about 77 MeV. From these data one can evaluate for each crystal the voltage V to get a gain $G=10^6$. Then a cosmic run is performed, by acquiring typically 10^4 events at 0.5 Hz trigger rate. An automatic procedure fits the cosmic peak to find Q and extract the PeY. The whole procedure is repeated then with a different value of the gain ($9x10^5$) as an independent cross check of the PeY value, which, of course, does not depend on the gain.

1.1.3.3.4 Response Equalization

Given the gain curve G(V) and the PeY for a block one can estimate for each lead-glass counter the working point V_{eq} , i.e. the voltage needed to get equal response for MIP's. After this first estimate the response equalization is cross-checked and fine tuned in a new cosmic run by fixing an arbitrary value of Q = 4.5 pC and adjusting the PMT voltage according to the estimation. If the equalization is not satisfactory a small change along the G(V) curve is done to improve it and an additional run is done to check if good equalization is achieved. Results for PeY's of about 200 blocks measured for the LAV-1 and for the spread of the equalized responses are shown in Figure 10 and Figure 11.

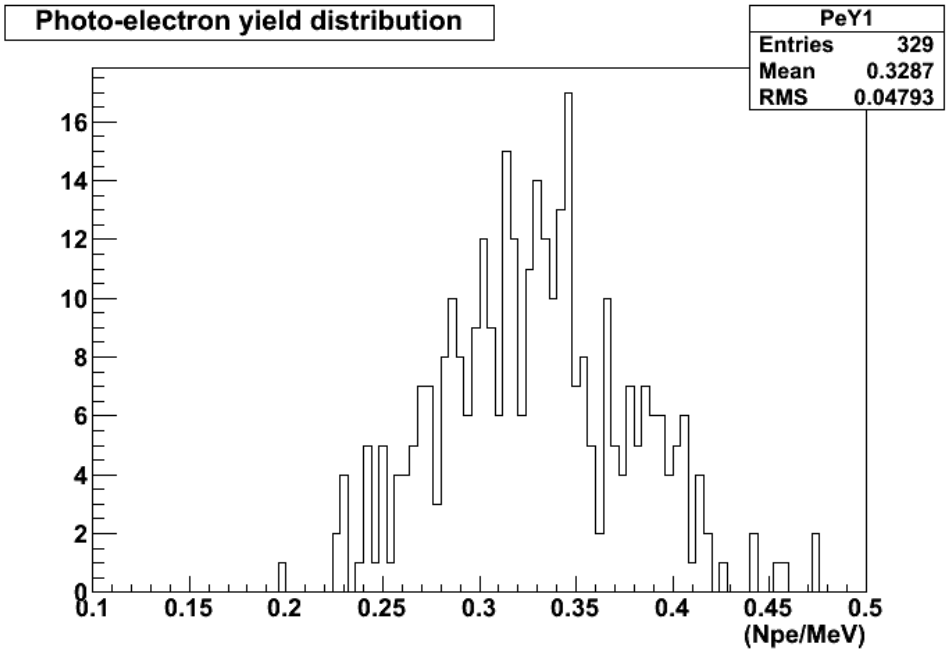

Figure 10 Photoelectron Yield (PeY) for a typical set of blocks

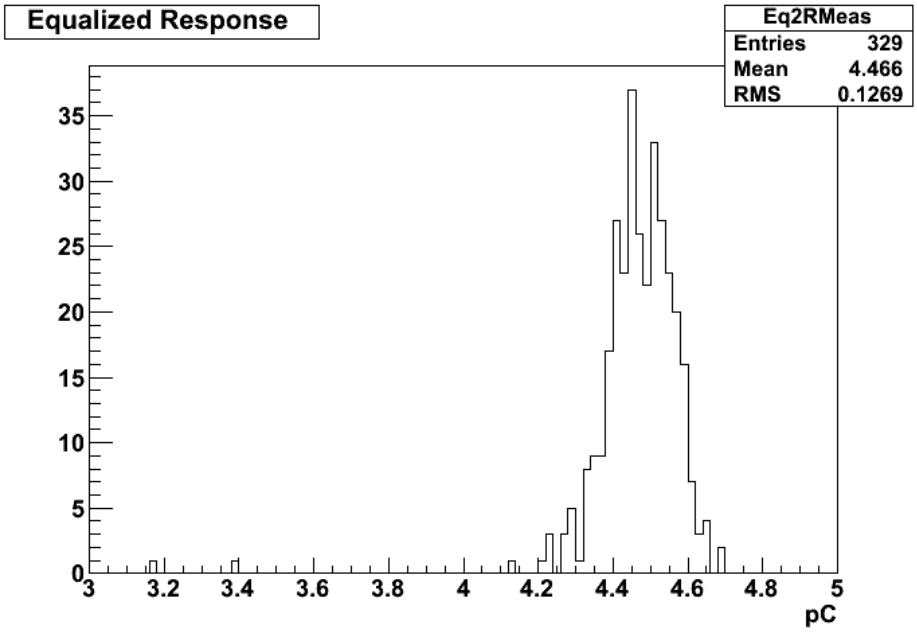

Figure 11 Spread of the equalized response for a typical set of blocks

1.1.3.4 Operation in Vacuum

The interaction of the beam with residual gas in the decay tube can produce a photon-free background to $K^+ \rightarrow \pi^+ \nu\nu$ that will become important if the vacuum is worse than 10^{-6} mbar in the fiducial region and worse than 10^{-5} mbar the downstream region of the spectrometer. The Large Angle Veto system must be able to operate inside the vacuum environment. The choice of having both the lead glass blocks and the PMTs inside the vacuum simplifies the design of the mechanics. In this context, it is important to note that the PMTs when used in OPAL were never operated in vacuum.

To validate the technological choices and the materials used a series of outgassing measurements were done. Heating tests for the voltage divider have been made to confirm the vacuum operation of the PMTs.

1.1.3.4.1 PMT Heating Test and Measurements

Two independent checks were done in Frascati and Pisa using vacuum vessels with infrared-transparent windows and a thermocamera. The results are described in the following.

The Hamamatsu R2238 PMT voltage divider has a maximum resistance R1=480 KΩ between the cathode and the first dynode which dissipates ~100 mW during operation. When the PMT is operated in air the power is dissipated through convection mechanism using air as medium. Once in vacuum the only possibility is through radiation and conduction. Figure 12 shows a picture of the PMT base made at a pressure of few 10^{-4} mbar using an infrared termocamera.

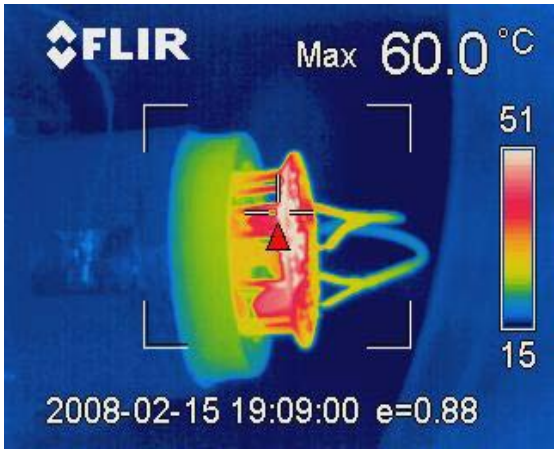

Figure 12 Measurement in vacuum of the temperature of the divider connected to the PM

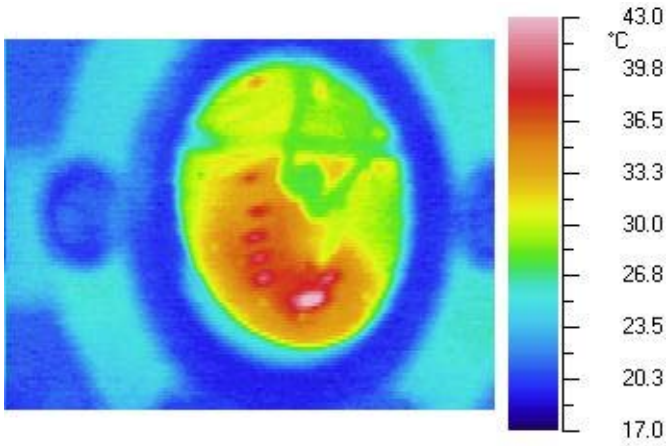

Figure 13 Measurement of the divider temperature in vacuum

The base reaches a maximum temperature of 60° C at the R1 resistor after more than 4 hours of PMT operation in vacuum. The picture shows that in addition to the radiative cooling, a conduction mechanism is active through the base connections to the PMT.

A similar test was performed in Pisa using the divider alone (without connections to the PMT) with an applied voltage of 1500 V in vacuum. Figure 13 and shows the results: the thermo camera was looking at the sample through a CaF_2 window and a calibration correction should be applied to the displayed temperature. With this correction, the temperature of the hottest point was found to be 70 ^{0}C, in agreement with the result from the test in Frascati.

To monitor the divider temperatures on a long time scale, PT100 temperature probes have been installed on R1 in more than 30 PMT dividers in the LAV 1 module. The temperature will be monitored during months of operation to spot unexpected behaviors.

1.1.3.4.2 Outgassing Measurements

Two methods were used to assess the outgassing rates:

- measure the vacuum pressure limit at known pumping speed
- measure the pressure rise time without pumping.

Details on how the measurements have been performed can be found in (5).

The use of two redundant measurements has allowed us to cross-check the results and to evaluate some systematic effects. The following notations will be used:

- Q_S: outgassing rate of the sample under investigation (mbar*l/s);
- Q: specific outgassing rate, i.e., the outgassing per cm^2 ($Q=Q_S=A$).

The outgassing rates for individual parts of the lead-glass detectors have been measured in a small vacuum chamber. The samples were pumped until the pressure became stable. After that the limit

pressure and the pressure rise time were measured. Details on the experimental setup can be found in (6). There is no evidence of significant contributions to the outgassing from the wrapping, the glue and the PMTs. The observed outgassing seems to arise mainly from water and air absorbed by the crystals. A conservative estimate of the single block outgassing rate is $Q_{BLOCK} = (7\pm10)\cdot10^{-6}$ mbar l/s after two weeks of pumping time.

The vessel of the first LAV module was tested for vacuum leaks using a helium leak detector with a limit sensitivity of $5\cdot10^{-11}$ mbar l/s. A limit of $< 1\cdot10^{-10}$ mbar l/s can be set on the leak rate for the vessel, 4 orders of magnitude lower with respect to normal operation pressure. To measure the outgassing rate the vessel was pumped for 96 hours reaching an ultimate pressure of $P_{lim} = (1.4\pm0.3)\cdot10^{-6}$ mbar. The result yields a total outgassing rate for the LAV 1 module of $Q_S = (1.1 \pm 0.2)\cdot10^{-5}$ mbar l/s, from which the specific outgassing rate of the vessel can be computed to be $Q = (0.9\pm0.2)\cdot10^{-10}$ mbar l/s/cm^2.

The outgassing of the LAV 1 vessel can be compared with preliminary estimates obtained at CERN for the NA48 vacuum tank, which has a specific outgassing rate $Q \sim 1$ to $3\cdot10^{-9}$ mbar l/s·cm^2 after 15 days of pumping time, while the LAV 1 vessel reaches $Q \sim 1\cdot10^{-10}$ mbar*l/s·cm^2 after only 4 days. The difference is most probably due to the fact that the inside walls of the NA48 vacuum tank are painted.

As a final consideration, the contributions to the overall outgassing rate from each of the components of the LAV 1 prototype are listed in Table 5. The estimates are obtained by scaling the measurements for each component to the amount used in the assembly of the entire LAV 1. For the outgassing of the blocks, both the worst case ($Q_S = (2\cdot10^{-5})$mbar l/s) and the average ($Q_S = (1\cdot10^{-5})$ mbar l/s) outgassing rates are listed.

Table 5 Estimated outgassing rate (mbar l/s) of LAV 1 with 160 lead-glass blocks

	Outgassing rate	*Days of pumping*
LG detectors (worst case)	$(2.9\pm2.0)\cdot10^{-3}$	15
LG detectors (average)	$(1.5\pm1.0)\cdot10^{-3}$	15
Monitoring system	$(1.0\pm0.2)\cdot10^{-5}$	15
Tyvek wrapping	$(3.1\pm0.6)\cdot10^{-5}$	5
LAV 1 vessel	$(1.1\pm0.2)\cdot10^{-5}$	4
Total LAV 1 (average)	$(1.5\pm1.0)\cdot10^{-3}$	15

Table 5 shows that the dominant contribution to the LAV 1 outgassing rate comes from the blocks. The contribution to the outgassing rate from the hardware and aluminum plates used to fix the blocks to the wall of the vessel is not included in the computation because it is considered to be small compared to the contribution from the blocks. The estimated outgassing rate of LAV 1 is $(1\text{-}2)\cdot10^{-3}$mbar l/s. A first measurement of the outgassing rate of the fully assembled LAV 1, based only on 7 days of pumping time, produced a value of $< 4\cdot10^{-3}$mbar l/s in reasonable agreement with the prediction based on single block measurements.

Using LAV 1 value a preliminary estimate of the outgassing rate for all the Large Angle Veto stations in vacuum, consisting of 11 rings for a total of about 2250 lead-glass blocks, is $(2\text{-}5)\cdot10^{-2}$ mbar l/s. This value is very similar to that obtained at CERN for the entire NA48 vacuum tank, $(1\text{-}5)\cdot10^{-2}$ mbar l/s.

1.1.3.5 Light Calibration

The LAV system must be accurately monitored given the demanding efficiency requirements. For instance, a 5-10% drop in efficiency in 1% of the blocks could produce effects of the same order of magnitude as the maximum allowed inefficiency of the system. In practice one will use software and hardware thresholds to flag an event, and thus a precise monitoring of the detector response is needed. The light pulse calibration system will allow checking of the response of each block to light pulses at any time in a simple and effective way. It will also allow checking of the stability of the PMT gain by repeating the procedure described in 1.1.3.3. Furthermore, when combined with the measurement of the response to beam halo muons, it will check the stability of the PeY (as defined in 1.1.3.3.3). It will also be useful to inter-calibrate the timings of the blocks.

The layout of the system is shown in Figure 14. It is composed of a light distribution system, based on silica fibres with different core diameters (see 1.1.3.6.7) and a remotely controlled LED pulser.

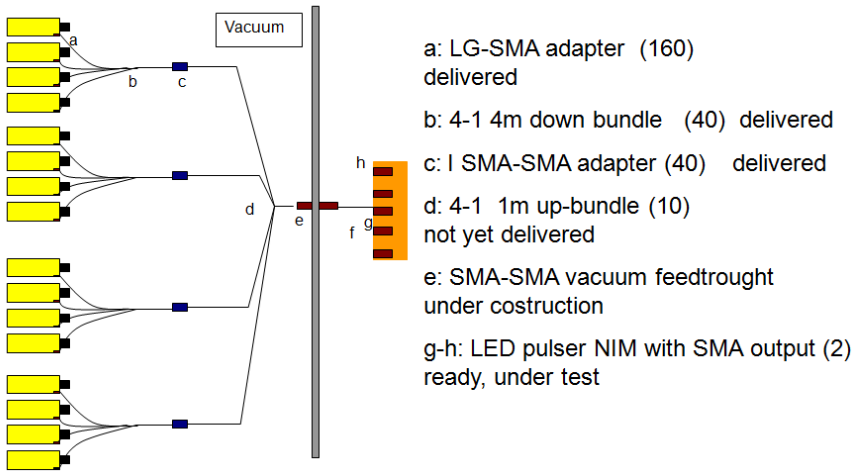

Figure 14 Layout of the fiber calibration system

Each LED pulser module can pulse independently 5 LEDs. Each LED is independently temperature stabilized at the level of 0.1 °C by means of a Peltier cell. The working condition can be software adjusted. The module has TCP/IP communication protocol and has both Ethernet and RS-232 connections. The pulser modules have been engineered both as standard NIM crate modules and as standalone devices.

Pulses can be generated via internal or external triggers at a maximum rate of about 500 Hz. They can be externally triggered in the inter bunch time (as done for the LKR system) for fast calibration purposes, and/or gain measurements.

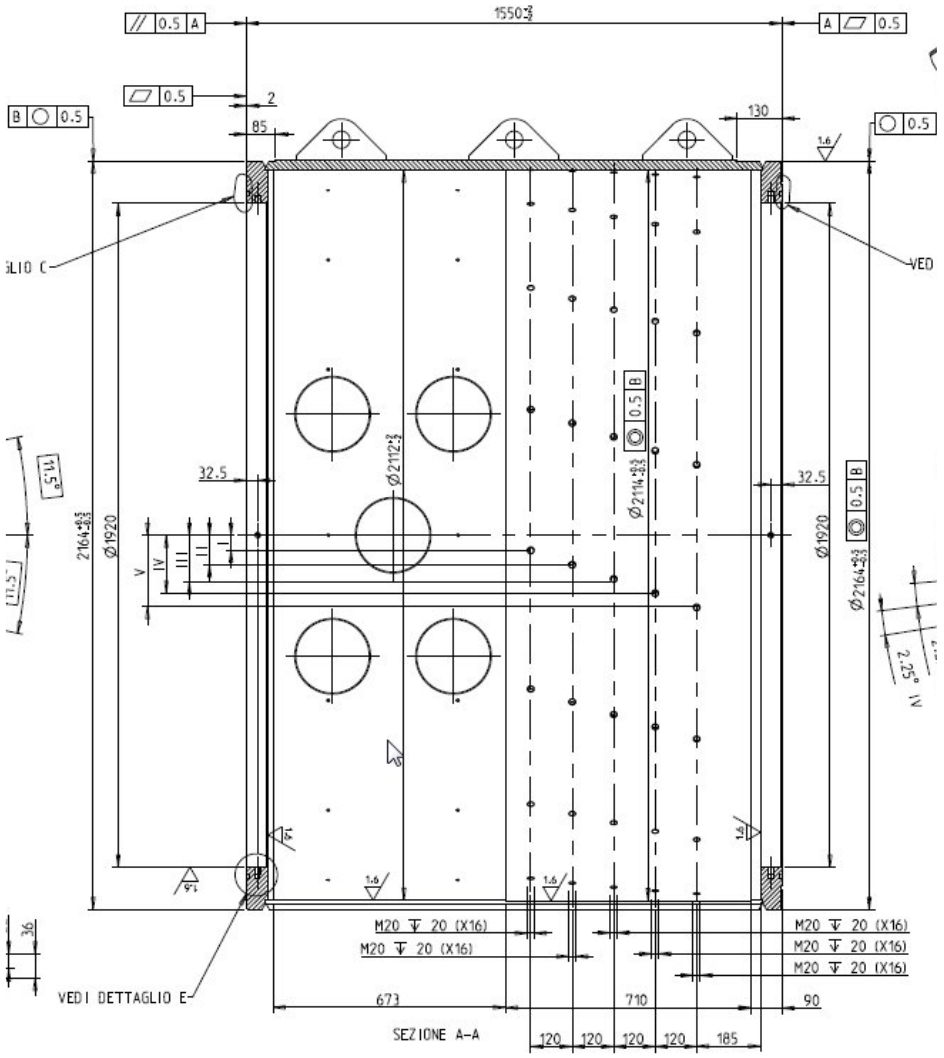

Figure 15 Lateral view of the LAV 1 vacuum vessel

1.1.3.6 Mechanics

1.1.3.6.1 Support Tubes

The detector crystals of the NA62 Large Angle Vetoes are contained inside a flanged vacuum vessel that supports the full weight. The overall dimensions of the different LAV vessels are listed in Table 6 and their longitudinal positions (the downstream ends) are listed in Table 7.

Table 6 Overall dimensions of the LAV modules

Station	Ext. Vessel Ø [mm]	Int. Vessel Ø [mm]	Int. Lead Glass Ø [mm]	Length [mm]	Total weight [kg]
1-5	2164	2114	1064	1550	~10000
6-8	2650	2590	1544	1550	~15000
9-11	TBD	TBD	1944	1430	TBD
12	TBD	TBD	2144	800	TBD

Table 7 Longitudinal positions of the LAV modules

Module	1	2	3	4	5	6
Longitudinal position [m]	122.220	129.830	137.440	145.050	152.660	166.170
Module	7	8	9	10	11	12
Longitudinal position [m]	173.680	181.190	193.391	203.909	218.530	239.645

There are several requirements that must be taken into account for the design of the vessel: the accuracy of the crystal position; the compatibility with the existing vacuum tubes; the vacuum tightness, cleanliness, outgassing, and the pumping & vacuum instrumentation; the cabling & feed-through flanges; the handling attachments; the mechanical strength; the tube attachments; the accessibility of the equipment inside.

The required accuracy for the positioning of the crystals is 1 mm. The inner diameter is accurate to +/-0.5 5mm with respect to the reference diameters listed in Table 6 and it is concentric to the two external flanges to 0.5 mm. Measuring the position of the externally machined flanges allows the determination of the crystal position. Eighty blind M20 holes are used to fix the crystal azimuth elements to the internal surface of the vessel (Figure 15). The compatibility with the existing vacuum tubes requires the same diameter for the bolting circle and the same diameter for the o-ring contact region. The height from the floor to the axis of the vacuum tube must also be respected. In order to have the correct mounting circle for the crystal, a reverse flange design was adopted (Figure 15).

It is important to ensure a good leak tightness on the interface flanges between the LAV vessel and the vacuum tank whilst respecting the mechanical tolerances of the flanges and the O-ring (Viton) grooves.

Five vacuum flanges, K200, for cable feed-throughs are positioned on one side of the vessels. A man hole (flange K630) is positioned either on the opposite side (stations 1-5) or on below the horizontal plane at an angle of about 45 degrees (stations 5-11) of the vessel (see Figure 16).

The manhole gives the necessary access to the inside and it allows to branch a large diameter pumping port. The inside surface of the vessel is equipped with a stainless steel grid to which the cables can be attached (see Figure 16). The handling of the vessel is assured by three lug attachments on the top. The total weight of the detector stations ranges between 9 and 10 tonnes.

It has been verified that the vessel, if open and with no cover, does not deform from its circular shape ($\Delta R < 2.5$ mm). The stress is also kept to a reasonable level for the material used, carbon structural steel 1.0044 EN10028-7 EN10025 (1993) S275JR Fe430B EN10025 (1990).

The construction and welding rules were reported in the PED code and must be followed. The design has been carried out using the standard PED EN13445. The qualification test and control will also be made using this standard. The design external pressure is 1 bar at a temperature of 20^0C. For this reason it is necessary to provide covers for all openings in order to perform vacuum tests. During construction vacuum tests were made after the tube was welded and prior to the final machining.

The test was then repeated after machining. The vessel is supported by four feet located at 30 degrees from the vertical axis of the cylinder (Figure 16). The tube, when supported by the four feet and with the detector weight, has a sag of 0.2mm.

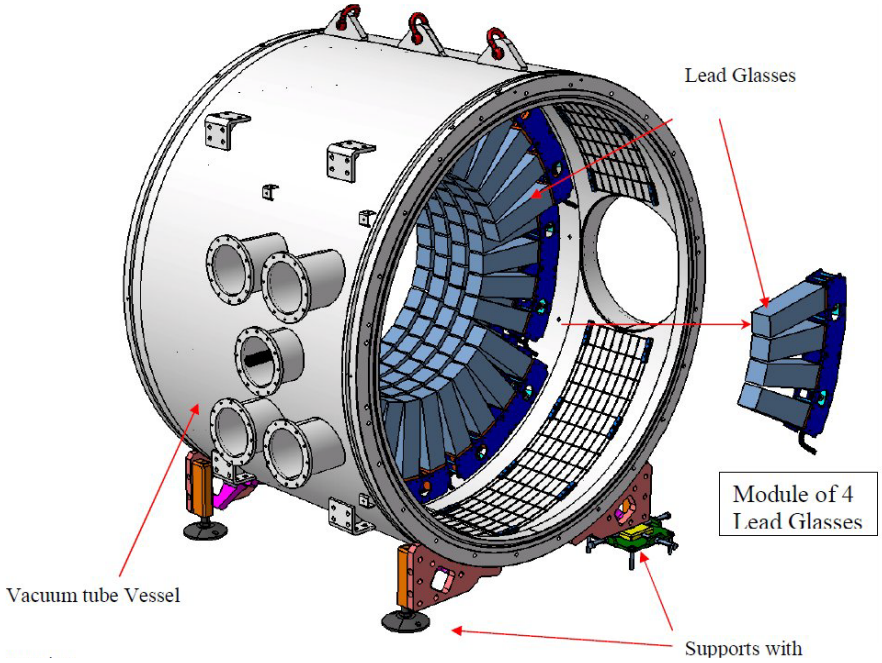

Figure 16 Complete station layout.

1.1.3.6.2 Support Structure for an Azimuth Crystal Segment

The structure supporting the crystals is made mainly by two aluminum plates connected together by spacers (Figure 17).

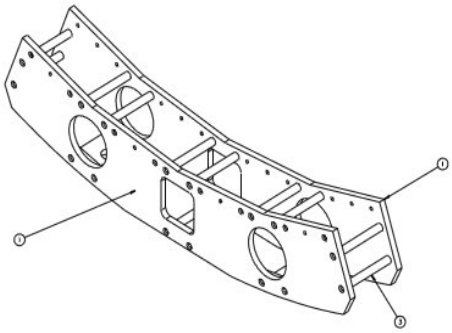

Figure 17 The support structure for one azimuth segment holding four crystals.

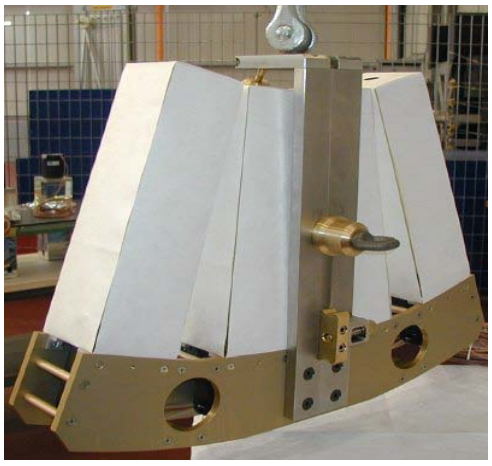

Figure 18 A complete azimuth segment hanging vertically

Four crystals are mounted to this aluminum structure by fixing the 1 cm stainless steel plates mounted on the crystal to the aluminum. The connection between the crystals and the stainless steel plates has been reinforced by gluing four stainless steel strips (106x26 mm, 0.3 mm thick) across the junction between the two elements, on the outside of the counter assembly (Figure 19).

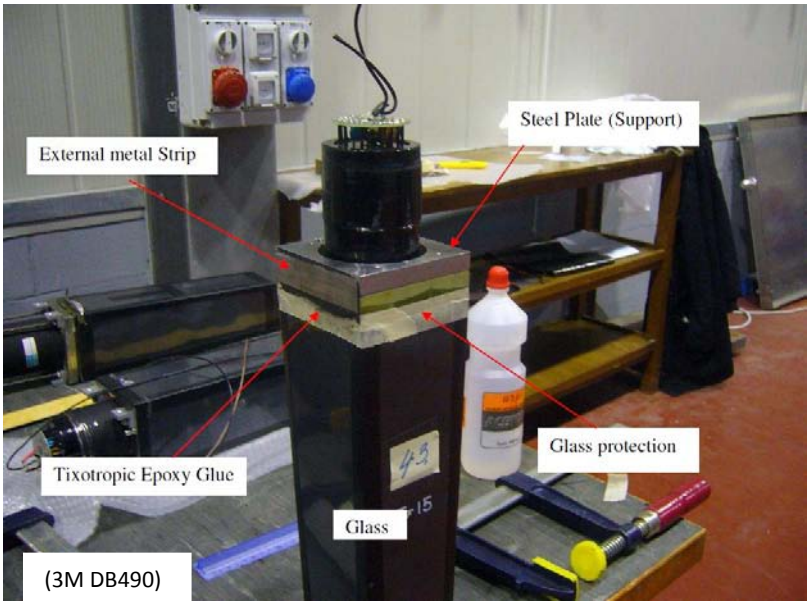

Figure 19 Reinforcement plates on a lead glass block

The two lateral plates contain two circular holes on the side; these give access to tightening the screws to attach it to the tube. The third square hole in the centre is used to handle the four crystals for the installation (Figure 18 and Figure 20).

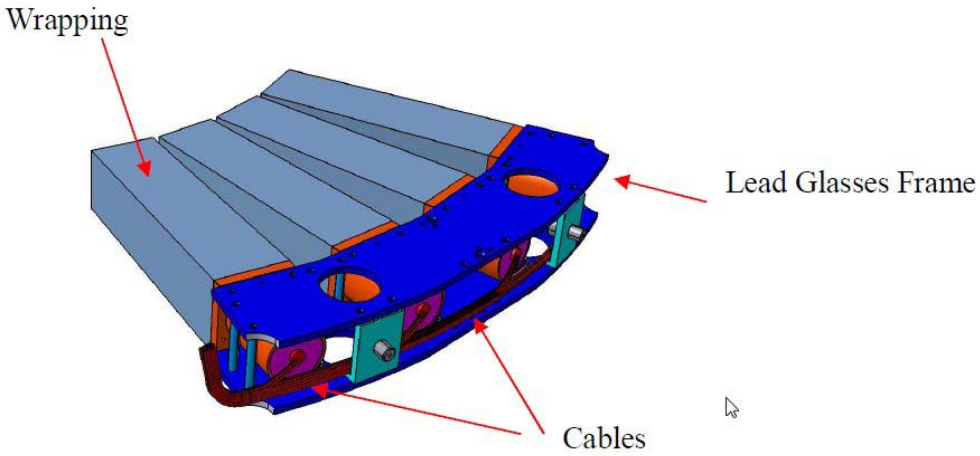

Figure 20 Schematics of the four-crystal assembly

1.1.3.6.3 Flanges

The connection between the internal signal cabling and the external electronics is to be made using 10 37/-pin, D-type CANNON connectors soldered onto a K200 flange. The signal ground is kept separate for each channel. This flange has been built with a custom configuration.

The connection between the internal HV cabling and the external high voltage power supply is to be made using eight 32-pin, MIL C-26482 type, round connectors soldered onto another K200 flange. It should be noted that the 32 pins are connected to 32 individual HV distributor channels. The HV cables will be grounded at the front end electronics crate. The ground connections for all channels will be tied together and connected to a dedicated feedthrough (one per layer).

The flange for the calibration fibres allows the coupling of the external optical fibres (600 μm core) to the internal bundles using SMA connectors. Both fibres face a polycarbonate window and both the internal and external SMA plugs can be finely positioned using small screws to maximize the light transmission. An appropriate O-ring ensures vacuum tightness.

1.1.3.6.4 Cable Routing

Inside a module, cables are routed first along each support structure to one of the short sides. Then the cable bundle (HV, signal and fibre) is laid along the space left between supports up to the section of the module where the grid for the cables has been mounted. The bundles are fastened to the grid in routings that permit each bundle to be properly terminate at its flange cable feed-through. An extra 20 cm of cable is left in the pipe to allow access to the connectors when dismounting the flange from outside.

1.1.3.6.5 Signals

As described in 1.1.3.2.2, the anode of the PMT is connected to a cable (whose length is a function of the radius of the ring) which has on the other side a crimped pin for the signal and the relative ground; these pins are inserted in a DB/37 connector that is connected directly to the flange.

1.1.3.6.6 High Voltage

To minimize material inside the vessel, the negative HV terminal of the PM distributor cable will be cut to length and terminated on the other side with a single pin to be inserted in a 32/pin MIL/C26482 connector, directly connected to the flange. The ground for each layer is grouped together and connected to a dedicated feedthrough.

1.1.3.6.7 Calibration Fibers

In each lead-glass detector the steel flange is equipped with a small hole, used in OPAL to inject light

for calibration and monitoring. The same hole is used for monitoring and calibration purposes. With respect to the one used by OPAL the connector has been changed to a standard commercial SMA connector. The scheme of the calibration system is sketched in Figure 14.

Light is injected in each block by a 200 μm core silica fibre. Fibres are grouped in bundles of four ("downstream bundles") supplying one azimuth segment, each bundle ending with a single SMA connector on one side and with four SMA connector on the blocks side. Each bundle is covered using Teflon, and the connectors are glued using EpoTeK 353 ND to reduce outgassing. For the small rings (ANTI 1-5) each downstream bundle is 4m long. Each downstream bundle is connected to one "upstream" fiber (400 μm core) using an I–shaped SMA connector, which is equally shaped and treated. They end with a with a single SMA connector on the vacuum flange. For the small rings (LAV 1-5) the upstream bundles are each 1m long. The routing of the fibres to the vacuum flange is the same as described for the HV and signal cables.

Externally the light is distributed by a 600 μm core silica fibre which is connected to the LED module. With this scheme, light generated by one LED is distributed to 16 blocks. The intensity of the LED pulser and the quality of the light couplings gives enough light output for our purposes at the end of the light distribution chain.

1.1.3.6.8 Temperature Probes

About 30 PT100 temperature probes are installed inside LAV 1 module, the major part on the hottest resistor in the divider and few on the plates glued to the glass. The purpose of this installation is to monitor the temperature rise in the divider and in the steel-glass junction (known to be delicate and sensible to temperature differences of some tens of degrees) and to possibly monitor the gain variation of the PMTs as a function of the temperature.

On the LAV 1 the connections to the outside readout have been done using spare signal pins (160 were used out of 256). For the other stations, one PT100 for each layer will be installed.

1.1.3.7 High Voltage System

The high voltage system is almost entirely based on the former OPAL HV distributors, powered by new HV power supplies. A specific controller board has been developed to integrate the control of the distributor in the CERN Detector Control System.

1.1.3.7.1 Power Supplies

One unit of the former OPAL HV distributors is a 19" chassis containing up to 15 HV distributor boards plus a controller one. Each board has 16 channels with individual DAC for voltage setting and individual series regulator for HV. The output setting of each channel can be read, after proper selection, through a specific HV connector on the front of the chassis. Each individual PMT high voltage can be set and regulate within a nominal voltage window of 510 V.

Each chassis can power up to 240 channels via output connectors on the back (55-pin round MIL C26482). One chassis will be used for each station, except for the last, where two chassis are needed.

The source power to each chassis will be provided by an ISEG HPn 20 757 power supply (2KV, 750mA max) controlled remotely by the experiment DCS.

1.1.3.8 Readout Electronics

1.1.3.8.1 Requirements

The LAV system will mainly detect photons from kaon decays, as well as muons and pions in the beam halo. For each incoming particles the veto detectors are expected to provide a time measurement, with a ~1 ns resolution, and an energy measurement with a moderate precision of order 10%. The system should be able to operate with very low threshold, well below one minimum ionizing particle (MIP), in order to keep the detection efficiency for muons and low energy photons as high as possible.

The simplest approach would be to split the signal from the PMTs of the lead-glasses in order to have:

- A fast measurement of the charge of the signal, using Flash ADC's or wave-form sampling;
- A fast digitization of the signal, using a discriminator and a TDC for time measurement.

The intrinsic time resolution of the lead-glass blocks (<1ns) and the rise time of the Hamamatsu R2238 PMT (~5 ns) do not put stringent requirements on the time measurement accuracy. On the other hand, the expected energy deposit in the LAV stations from photons coming from π^0 decays covers a very wide range, from ~10 MeV up to 30 GeV as shown in 1.1.1. As a reference, the PMT signal for a cosmic ray muon is shown in Figure 21.

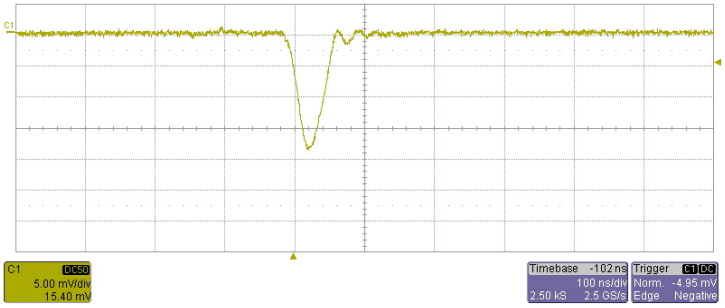

Figure 21 Typical signal from cosmic ray muons

This wide photon energy range, together with the necessity of detecting muon signals, requires operating the R2238 PMTs at a gain of order 10^6. Using the measured average photoelectron yield of 0.3 p.e./MeV, one expects a ~4.5 pC charge for a MIP, corresponding to a signal amplitude of ~20 mV over 50Ω. On the upper part of the range, signals from 20 GeV showers can reach an amplitude of 10V over 50Ω. Such a signal range would be outside the possibilities of commonly used ADC chips, whose dynamic range is at most 50. On the other hand, the range of a typical amplifier-shaper-discriminator chain is of order 10.

In selecting the readout scheme, the cost and data through-put must also be considered. An approach using Flash ADCs is more expensive as the modularity of channels per readout board is low. In addition, it needs shaping electronics to stretch the signal slightly in order to have a reasonable number of samples at 40 Mhz and it imposes huge constraints on the readout board as far as the data throughput handling is concerned.

We have identified three possible strategies to cope with the wide signal amplitude range, while keeping under control the cost and complexity of the system:

- Use a front end electronics with a clamping stage followed by an amplifier;
- Use of multiple scales with different amplification factors for the same input signal;
- Measure the signal height using the Time over Threshold (ToT) technique.

The requirement of signals as high as few Volts rules out most part of commonly used ASIC produced for HEP applications, such as CARIOCA, NINO, ASDQ, etc. On the other hand, the application does not justify the effort of producing a new dedicated ASIC. The idea is then to use commercial amplifier and comparator circuits, to produce a digital output signal with time duration equal to that of the analog input, exploiting the advantage of having high amplitude signals and a relatively slow rise time. Using this technique, the resulting dynamical range of the input signal is enlarged, due to the typical non-linear relationship between the ToT width and the input signal amplitude.

1.1.3.8.2 The LAV readout chain

The output signals from each station are connected to 32 channels front end electronics (FEE) cards. These FEE cards convert the analog signal from the PMTs to a digital signal of proper width (equal to the ToT duration) using the differential LVDS standard. Then, the digital signal time of arrival and width are measured by TDC daughter-boards (using the HPTDC as described in section **Error! Reference source not found.** on page **Error! Bookmark not defined.**) mounted on a TEL62 board. The FPGA inside the TEL62 produces the time corrected from the slewing introduced by the discriminator, using a double threshold system (described in the following paragraphs), and the charge for each hit reconstructed from the ToT width and a time-charge calibration. This information is then sent to the following DAQ stages. L0 trigger primitives are calculated inside the TEL62 and sent to the Level 0 supervisor. The general layout is shown in Figure 22.

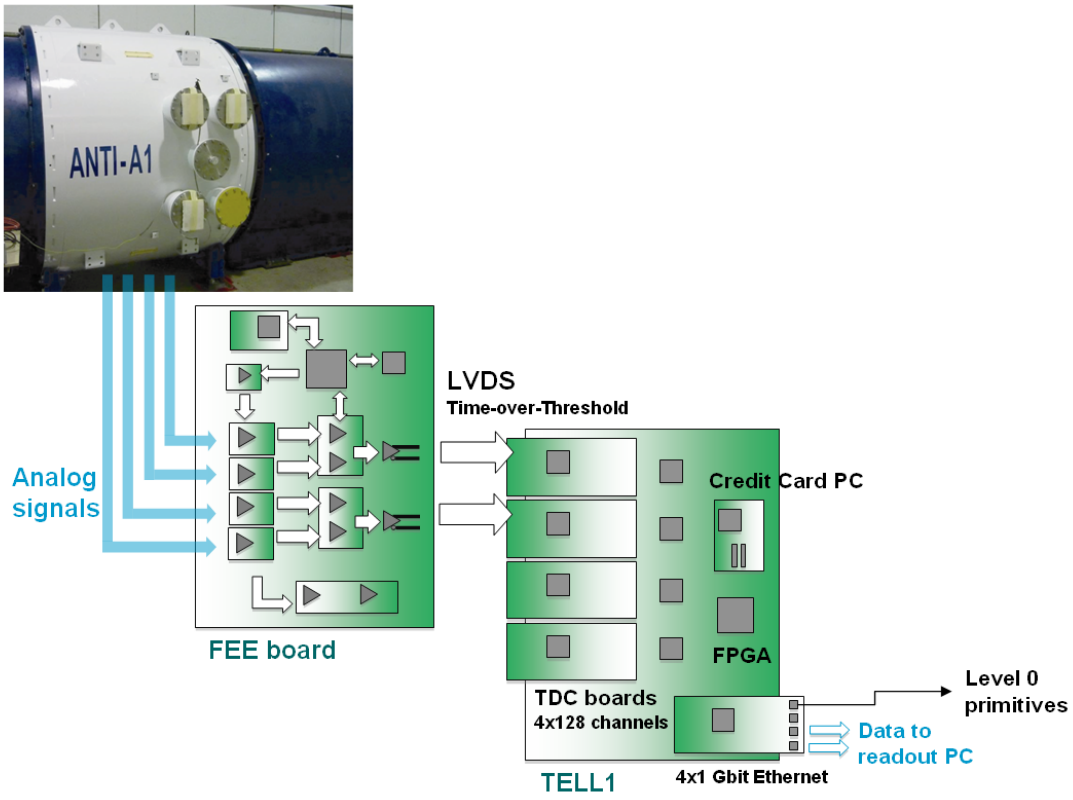

Figure 22 Schematic scheme of the LAV readout (for one station).

1.1.3.8.3 Frontend Electronics

The most specific part of the LAV readout is the dedicated FEE card. This is a custom project designed to convert the analog signal coming from the PMT into an LVDS digital signal of the same width. The analog input signal is clamped to avoid too large input signal to the amplifier stage. The analog signal is then amplified, split and send to two separated comparators (Figure 23). Each of them compare the analog with a programmable threshold and produce an LVDS output signal whose width is equal to the time the analog is above threshold.

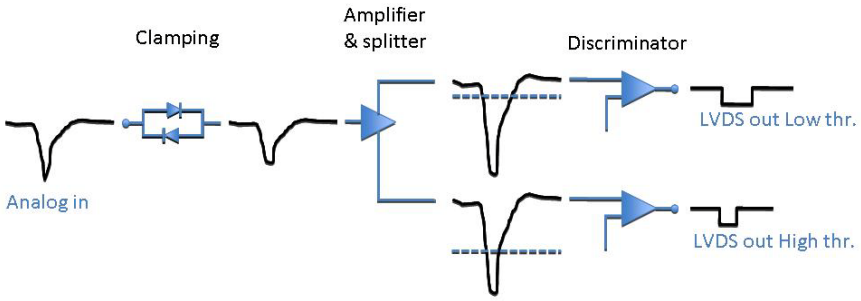

Figure 23 Basic functionality of one channel

The LVDS signal is then transmitted to a TDC to measure its width that is related to the deposited charge. The functional relation between ToT and charge is logarithmic and therefore saturates for

high charge values decreasing the sensitivity of the reconstruction algorithm. The use of a second threshold crossing the top part of the PMT signal, where the slope is steeper, allows to extend the range of sensitivity. A detailed description of the FEE functionality will be given in the following paragraphs. A single channel layout is shown in Figure 24. Each board will house 32 analog input channels delivering 64 LVDS output to the TDC cards. The boards will also provide calibration signals and analog sums useful for the board diagnostic.

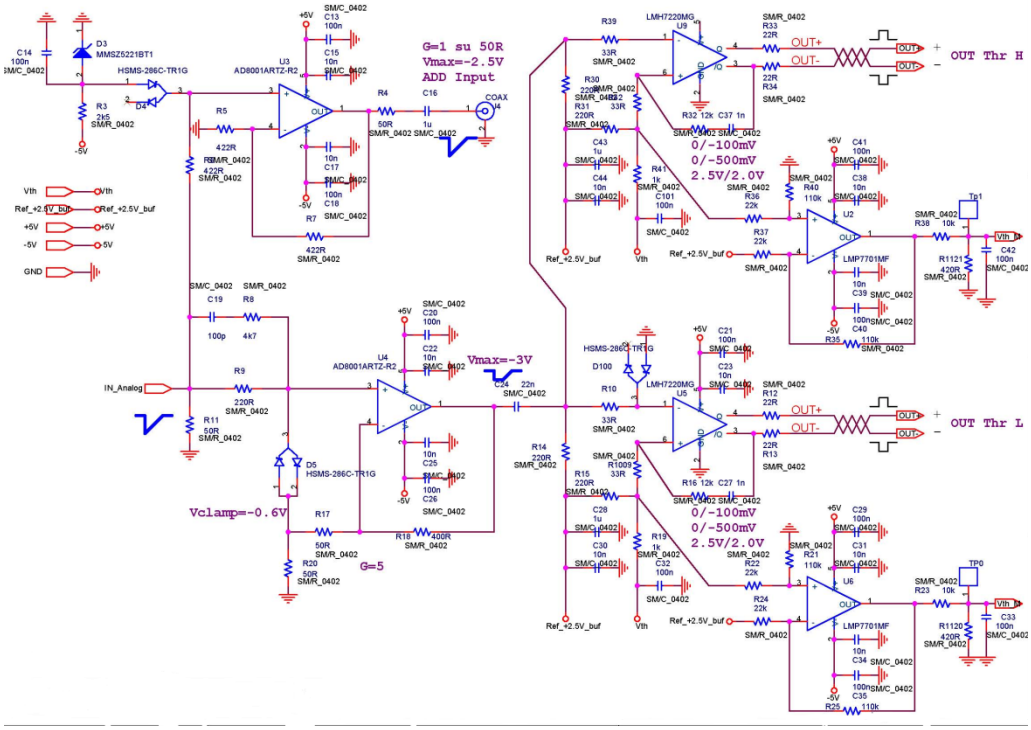

Figure 24 Single channel layout for Time-over-Threshold custom board

1.1.3.8.4 Clamping Stage

In order to protect the amplifier stage from too large signals, the input amplitude must be limited to a maximum of 600 mV in order not to exceed, after amplification, the maximum dynamic range of the comparator (~2V). The clamping circuit is designed to be able to sustain high signal rate up to 12 V, but is able to tolerate an isolated larger signal. To preserve the ToT measurement, the clamp circuit must cut the edge of the signal without changing its time duration. This is achieved by using a couple of very fast low capacitance Schottky diodes (type H5M5-286C-TR1G). The clamping performance has been simulated and the results are shown in Figure 25.

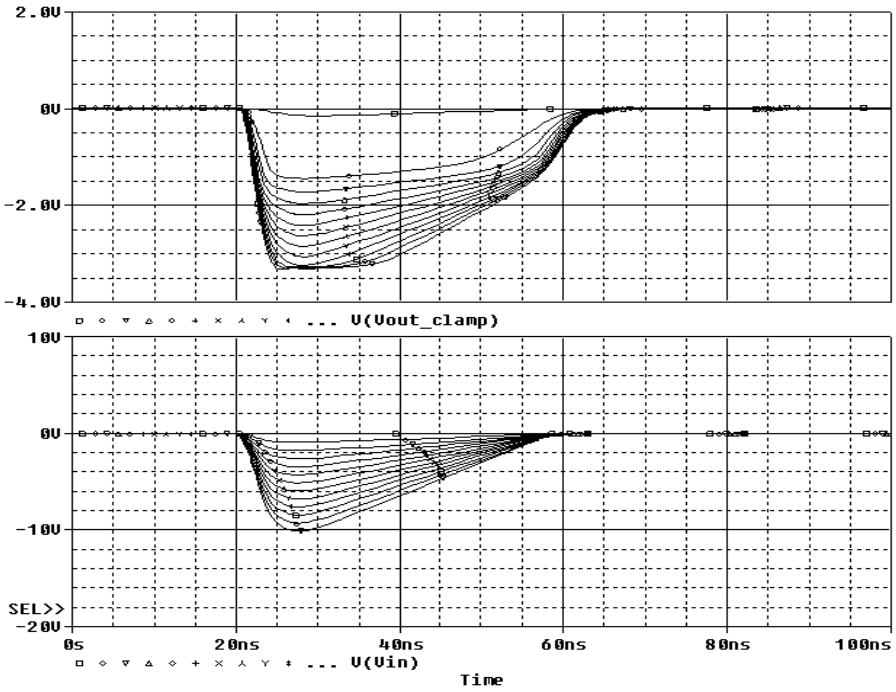

Figure 25 Clamping stage simulation

The figure shows how, when changing the pulse-height of the input signal (bottom) and maintaining the same time basis, the clamping circuit produces a response (top) with clamped output amplitude, but with unchanged time width. To avoid diode breakdown due to excessive heating, appropriate dissipative pads are inserted on the printed circuit board.

1.1.3.8.5 Amplifier

The ToT system should work with a very low effective threshold on the analog signal in order to maximize efficiency. To improve signal to noise separation and reduce the walk dependence on the analog amplitude (overdrive), a moderate amplification is needed (we have chosen a gain of ~3). This also allows compensating the degradation of signal rise time due to the cable between the PMT and the FEE card (4.5 m inside the LAV station vessel plus a 1 to 2 m cable from the flange to the FEE card).

A high bandwidth, high speed Current Feedback Amplifier (type AD8001) is used for this purpose. After the decoupling capacitor C24, to avoid amplifier DC offset with a band of 50 KHz, the output is sent to the comparator input.

1.1.3.8.6 Comparator and LVDS driver

The amplified input signal is divided in two copies and each sent to LMH7220 High Speed Comparator with LVDS Output. This device compares the input with a programmable threshold which can be adjusted in the range 0-250 mV with a 12 bit resolution. To reduce double pulses at the comparator output, due to noise in the input signal, a 10 mV hysteresis is also provided. The comparator produces an output signal starting when the leading edge of the analog signal crosses

the threshold, and stopping when the trailing edge crosses the threshold again. This digital signal is transmitted to the TDC using the LVDS differential standard.

1.1.3.8.7 Analog Sum Circuits

In order to have the possibility to monitor the input analog signals to the FEE board, an analog output is required. Due to mechanical constraints it is impossible to have 32 analog output LEMO connections in the front panel. For that reason the single analog signal are collected in sums of four blocks (one azimuth segment) and then summed again in groups of four to get an half ring sum. The dynamic range of both the inputs and the sums is 2V. The board is equipped with 8 LEMO connection for the sum of 4 blocks, in yellow in the figure below, and two LEMO connection for the sum of a half quadrant, 16 blocks (Figure 26).

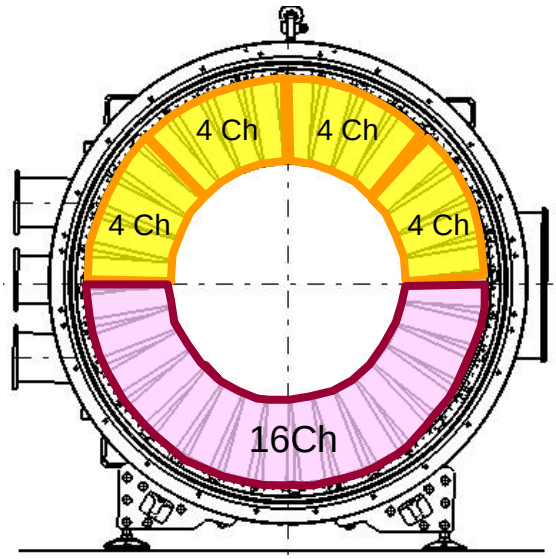

Figure 26 Layout of the analog sums

1.1.3.8.8 Test Pulse Generator

To diagnose electronics functionality, channels integrity and channels calibration, an internal pulse generator has been introduced into the FEE board. The pulse generator it is able to provide pulses with 10-50 ns programmable width, and 10-500 mV programmable amplitude using 12 bit words. The stability of the both amplitude and width is order 1% and the pulse rise time will be order 2 ns. The internal pulser can be triggered both locally, controlled by the on board CPU, or externally, using an external clock. To allow maximum flexibility the pattern of channels to be pulsed can be software programmed.

1.1.3.8.9 Test of the Prototype Boards at CERN

Five prototype boards, with 16 channels each, were produced during spring 2009 with the aim of validating the ToT technique. They have only 1 threshold, adjustable in group of 4 blocks using a trimmer, for each channel without all the control. The boards include an amplification stage with dual output: one copy of the signal is fed to the discriminator, which produces LVDS digital signals with time-over-threshold duration, while a second copy is available for routing to a different readout.

After the assembly of LAV 1 was completed at LNF in July 2009, the module was transported to CERN. It was installed in the existing NA48 vacuum vessel in October 2009.

The five prototype frontend boards were used to fully equip one half of the ring (80 crystals), so that we were able to perform extensive tests with muons and electrons using the SPS beam line. The second copy was used for direct charge measurements for the purposes of comparison.

For the charge measurement, we used commercial 12-bit charge QDCs (CAEN V792), while for the time measurements we used commercial TDCs (CAEN V1190B). The CAEN TDC is based on the CERN HPTDC chip which is the same used in the TDC boards built for the TEL62. In order to provide a gate for QDC integration, a trigger signal was provided by the fast-OR of the 16 digital signals in the upstream ring of lead-glass detectors. A stand-alone DAQ system was also prepared, capable of gating the acquisition with SPS status signals and sustaining a trigger rate of about 1 kHz. We collected large samples of data both with a diffuse halo of muons, thus illuminating all the counters in the ring, and with electron beams of energy 2, 4, and 6 GeV.

1.1.3.8.10 Charge Reconstruction Technique

The reconstruction of the charge of a single hit is based on the correlation between the charge and the Time-over-Threshold produced by our FEE card. This correlation is shown in Figure 27 for events collected during our tests with the cosmic ray setup.

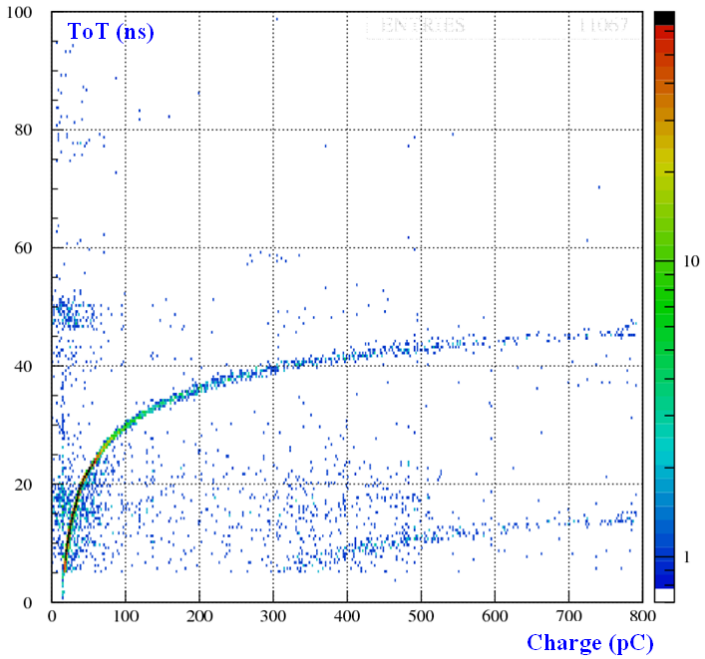

Figure 27 Correlation of ToT measurement and charge for cosmic muon signals

The distribution shows different behaviours in different parts of the spectrum:

- The curve shows signals with a very clean correlation over the entire charge range covered by our QDC (CAEN V792, 400 pC full range, 12 bits resolution)
- The PMT re-firings are identified as high charge and low ToT signals (in the right-bottom part of the plot)
- Noise in the PMT generates a halo of wrong charge events

The charge to ToT correlation also shows saturation at high charges, reducing the sensitivity of the measurement for very high signals. This is not an issue since we would in any case veto events with very high energy deposits in the LAV.

1.1.3.8.11 Charge Reconstruction Performance

The clear relation between the charge and the ToT shown in Figure 27 can be exploited to reconstruct the hit charge from the digital signal time width, namely the difference between leading and trailing edge times. In Figure 28 (left), the charge average value has been represented as function of the time width of the signal. The relation can be parameterized in first approximation with a 4th degree polynomial function:

$$Q_{REC}(pC) = p_1 + p_2\Delta t + p_3\Delta t^2 + p_4\Delta t^3 + p_5\Delta t^4 \qquad (1)$$

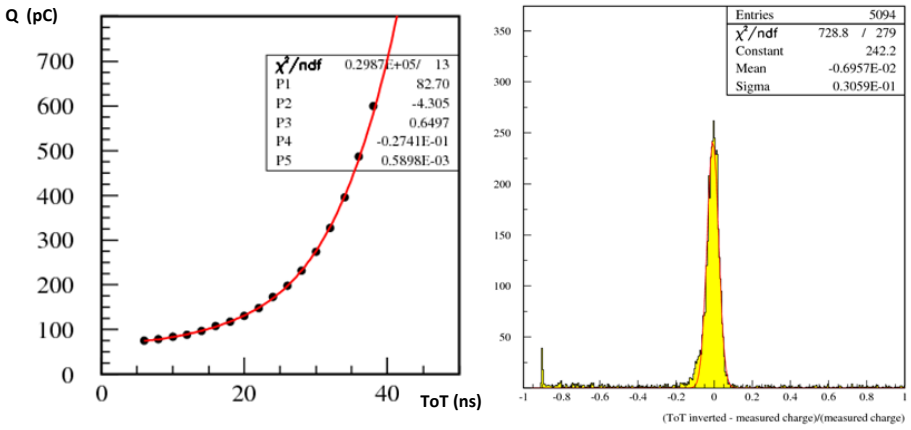

Figure 28 Left: Charge vs ToT. Right: Resolution of charge measurement using ToT

The fit result is superimposed in red. Using (1) and the parameters obtained from the fit, the reconstructed charge Q_{REC} can be calculated. The histogram on the right of Figure 28 represents the relative error on the reconstructed charge obtained with the formula:

$$\frac{\delta Q}{Q} = \frac{Q_{REC} - Q_{ADC}}{Q_{ADC}}$$

The Gaussian fit shows that the core resolution is ~3% and that there are very small tails in the reconstruction. The performances are very good, but we must remember that the charge range is essentially the low part of the spectrum, covering therefore the region of maximum sensitivity for the correlation function.

1.1.3.8.12 Time Resolution

The intrinsic time resolution of the lead-glass blocks has been estimated to be better than 700 ps using electrons during the first LAV prototype test beam in 2007 at the Frascati BTF, due mainly to light collection in the crystal. Nevertheless during operation at NA62 the wide range of signal amplitudes will introduce a considerable slewing, contributing worsening the single block time resolution. Estimates for 10 mV threshold and 5 ns rise-time indicate that the slewing effect can add up to 4 ns for small signals, and at least 2 ns for MIP signals. For this reason a slewing correction is needed in order to reach a good on-line time resolution. The correction can be easily computed once the charge of the hit is known. Due to the absence of direct charge measurement in the present project, the charge should be reconstructed using the ToT signal width, which is of course still affected by the slewing in the leading edge. This problem can be overcome by using a second threshold: the leading edge slope can be easily computed from the two threshold crossing times, and then used to improve the time measurement correcting for the slewing effect:

$$T_0 = T_L - L_{THR} \cdot \frac{T_H - T_L}{H_{THR} - L_{THR}}$$

Using the above formula the slewing corrected time of the hit, T_0, can be computed just using the values of the thresholds in mV, H_{TRH} L_{THR} , and the corresponding crossing time of the leading edge T_H T_L.

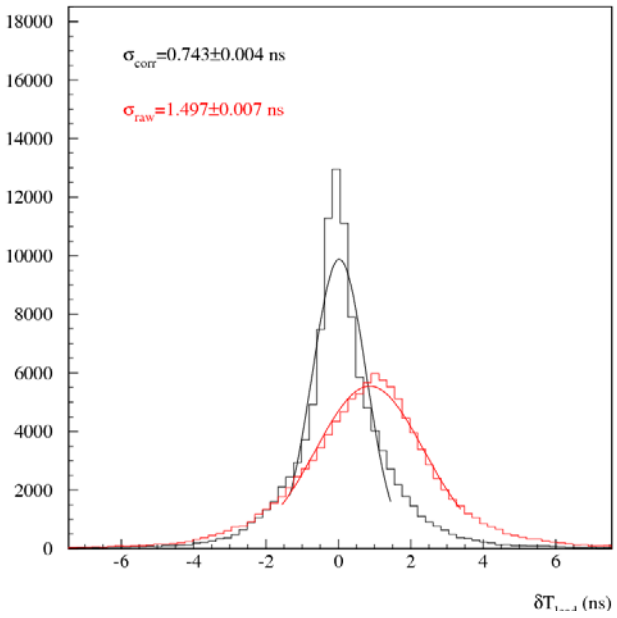

Figure 29 Time resolution with electrons

Figure 29 shows the distribution of hit's times of two blocks produced by 2 GeV electrons during the LAV test beam at CERN. The preliminary result of resolution for slewing corrected distribution in black is 750 ps with an improvement of a factor 2. The core resolution is better than 500 ps for a single block. For each particle crossing the LAV detectors there are many firing blocks allowing further improvements of the time resolution. Averaging all the block measurements a resolution ~300 ps for a MIP and ~150 ps for electrons and photons can be reached in each single station.

1.1.3.8.13 Improving Divider Performances

The correlation ToT vs charge shown in Figure 30 (right) below is obtained using 2 GeV electrons during the 2009 test at CERN of the LAV1 module with SPS beam. We discovered the presence of a discontinuity in the logarithmic relation due to a jump in the distribution of signal ToT, which can cause the charge reconstruction algorithm to fail. Figure 30 (left) shows the analog signal of one Hamamatsu R2238 PMT. The tube has a ringing following the main signal. This behavior has been observed already by Hamamatsu in the PMT datasheet.

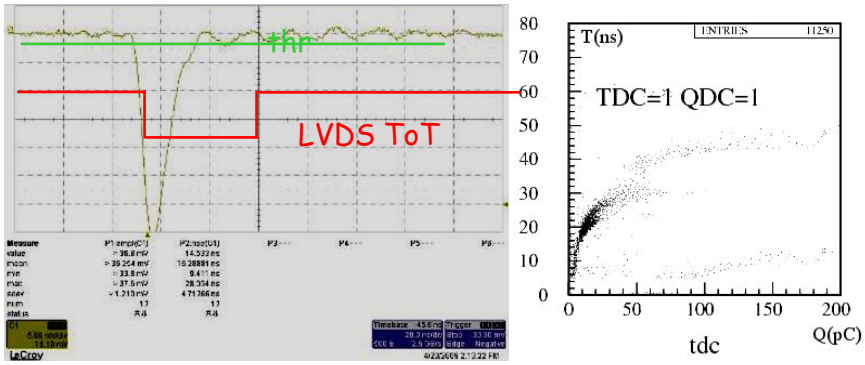

Figure 30 Left: Discriminated pulse – Right: ToT vs charge correlation

The ringing enlarges the LVDS signal, representing the ToT, as soon as it comes above the threshold. In fact, the TDC is unable to separate signals, such as the ToT ringing, that are narrower than 5ns, and therefore the ringing signal is merged with the LVDS of the main signal. After analyzing the PMT in detail we discovered that the ringing was due to parasitic inductance among the last 3 dynodes and the divider of the PMT. To quench the oscillating behavior we projected and built a modified divider including resistors on the last 3 dynodes (Figure 31).

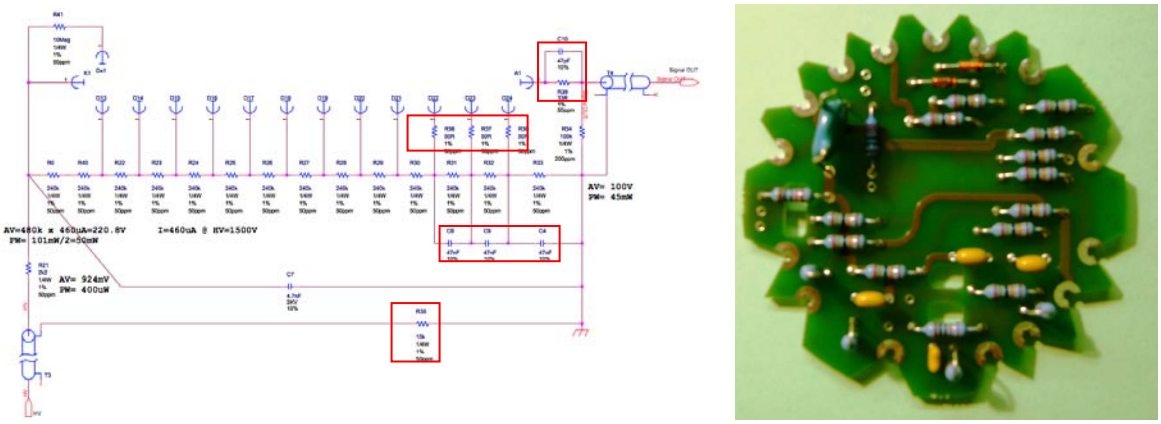

Figure 31 The new PM divider

These resistors are used to reduce the dumping coefficient of the circuit to ~1. The same technique has been also applied to the anode. The red boxes in Figure 31 above show the positions of the four resistors added, as well as of the capacitors in parallel to the last stages and the 10K resistor in the ground line to decouple HV and signal grounds. This solution cured the oscillations in the analog signals allowing us to improve the charge sensitivity of the ToT technique by a factor greater than three. We produced 2500 new dividers which will replace the original Hamamatsu ones. Test of gain and time characteristics of the PMT main signal show no changes with respect to old dividers.

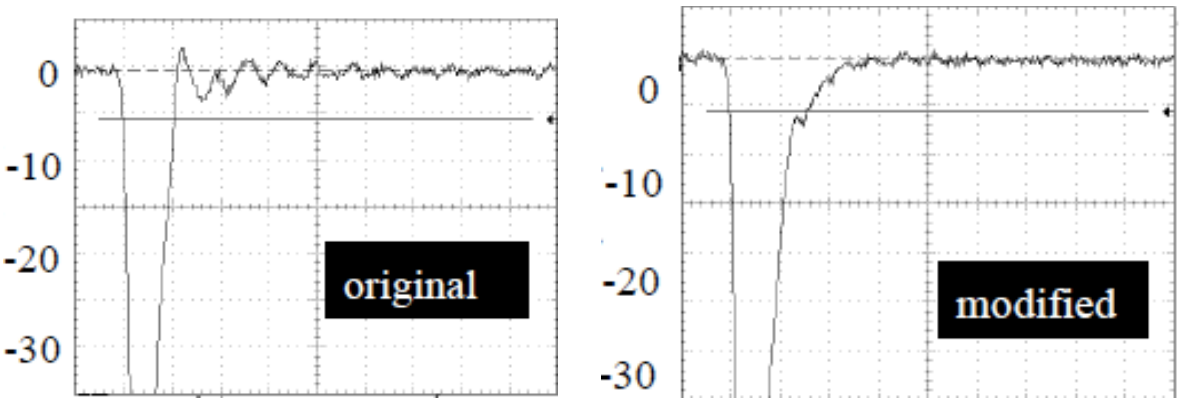

Figure 32 Difference of the signal between the old and new divider

Figure 32 above shows the difference between the original divider and modified divider signals. The ringing in the right part of the left figure is largely suppressed.

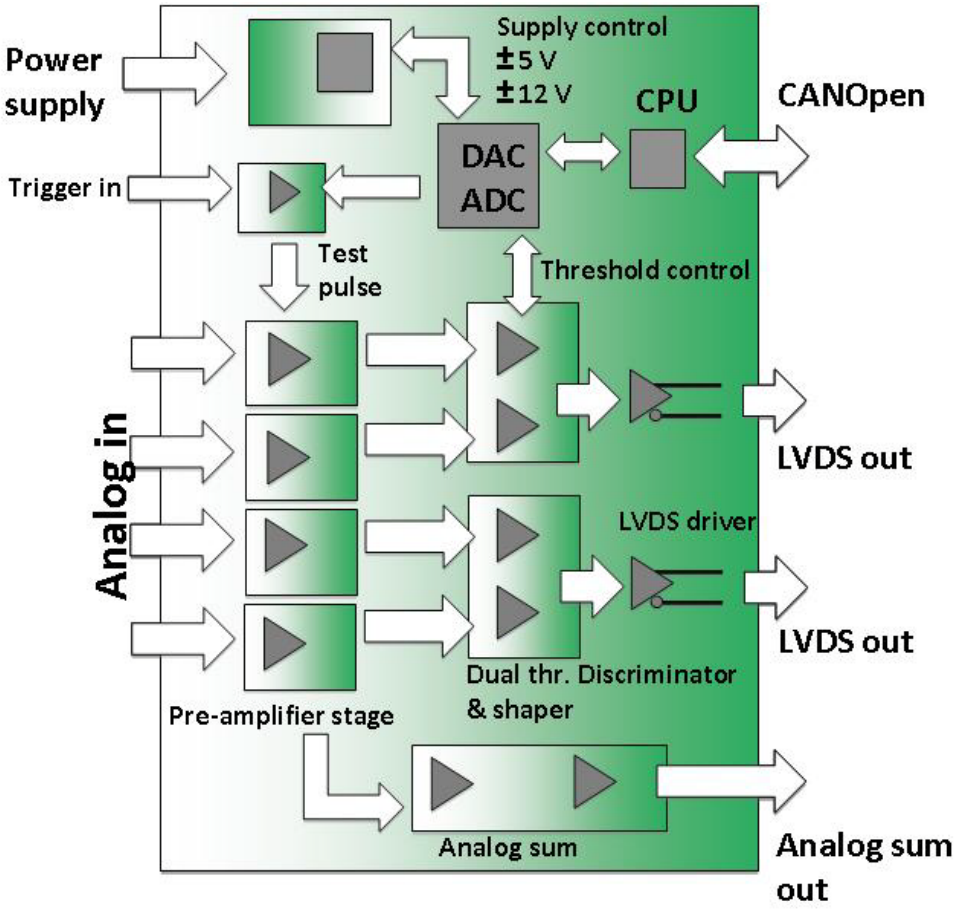

Figure 33 The layout of the frontend card

1.1.3.8.14 LAV Frontend Board Layout

The final LAV FEE card is a VME 9U board able to manage 32 analog input channels.

The input connection is made by two DB37 connectors, in which for each channel both the signal and its ground connection are transmitted. The general layout of the FEE card is shown in Figure 33.

Each board has a two x32 channels output LVDS connectors. The FEE board is connected to the TDC using two 34-Pair, 68-Conductor double-shielded SCSI cables.

The channel multiplicity is very easy to match due to the fact that each TDC daughter-board will allocate 4 connectors filling the 128 channels.

The FEE is made by different modules: the motherboard, which manages all input and output connections and the power supply, 16 daughter board housing 2 channels of the ToT discriminator electronics each, 8 daughter boards for the analog sums, and finally a daughter board housing the DAC and ADC and the slow controls. This design minimizes the cost in term of spare channels allowing to have many spare for the different daughter boards and a few spare for costly motherboards. The boards use standard VME 9U mechanics, 400x400 mm^2, with non-standard power supply ($\pm$7V, +3.3V, $\pm$12 V) and no VME bus. All the slow control and communication functions are implemented using CANOpen standard in agreement with present CERN standards

1.1.3.8.15 Crate for the LAV Frontend

In the present design of the LAV readout system each of the twelve stations will be equipped with a VME 9U non-standard crate housing and, depending on the type of LAV station involved, 1 TEL62 board (9U, 2 slots) and from five to eight front end boards. Moreover there is the possibility that from five to eight monitoring system cards will be placed in the same crate.

The FEE boards will need an extra $\pm$7 V power line and no standard VME bus. For that purpose we are currently considering the possibility to ask for a custom low cost version of the UEV 6021-LHC VME crate to be produced by Wiener. The cost reduction will be based on the substitution of the present 6U VME bus with a 3U J1 power bus only.

1.1.3.8.16 Number of Channels

The present readout scheme is based on three basic elements:

- FEE card (32 analog inputs, 64 LVDS outputs);
- TDC daughter board developed in Pisa (128 channels each), to be hosted on the TEL62;
- TEL62 readout board (can handle four TDC boards for a total of 512 channels)

We assume to use two different thresholds for each physical signal to allow online slewing correction, improve high charge sensitivity, and ensure redundancy in case of TDC broken channels. The presence of a second threshold will not change the number of FEE cards and TEL62 but only the number of TDC boards and cables are affected. In Table 8 the number of channels, the number of FEE cards, TDC cards, and TEL62 board is estimated for the whole veto system.

Table 8 Number of detectors and readout channels

Detector Station	N° of detectors/station	$N_{stations}$	N_{ch}	N_{FEE}	N_{TDC}	N_{TEL62}
1-5	160 (5x32)	5	800 x2	25	15	5
6-8	240 (5x48)	3	720 x2	24	12	3
9-11	240 (4x60)	3	720 x2	24	12	3
12	256 (4x64)	1	256 x2	8	4	1
Total	2496	12	4992	81	43	12

The table shows that we have ~2500 detectors with ~5000 readout channels. To equip the whole system around 85 FEE, 50 TDC boards, and 15 TEL62 are needed.

Each board has two 32 channel output LVDS connectors. The FEE boards are connected to the TDC using flat or round shielded cables with Robinson-Nugent 68 pin connectors. The channel multiplicity is very easy to match due to the fact that each TDC daughter-board will allocate 4 connectors filling the 128 channels. The connections to the TDC system are described in Section **Error! Reference source not found.** on page number **Error! Bookmark not defined.**.

1.1.3.9 Module Construction Phases

1.1.3.9.1 Assembly

The assembly area at LNF (Figure 34) is located in a newly constructed hangar building, with the following characteristics: the floor is capable of supporting the weight of the apparatus; an area to the right of the hangar doors has been fenced off for use as the NA62 experimental area; a 20-ton

overhead crane has been modified, together with the control unit, to ensure that operations can be carried out safely and at low speed.

Figure 34 The assembly area in Frascati

The assembly operations can be grouped into three phases:

- Preparation and installation of detectors into the cylinder
- Rotation and electrical and vacuum testing
- Packing for shipping

1.1.3.9.2 Preparation and installation of the Detectors into the Cylinder

Preparation of the blocks

The detectors are first removed from the shipping crates, by using a specially designed tool (Figure 35). A single detector weigths about 25 kg.

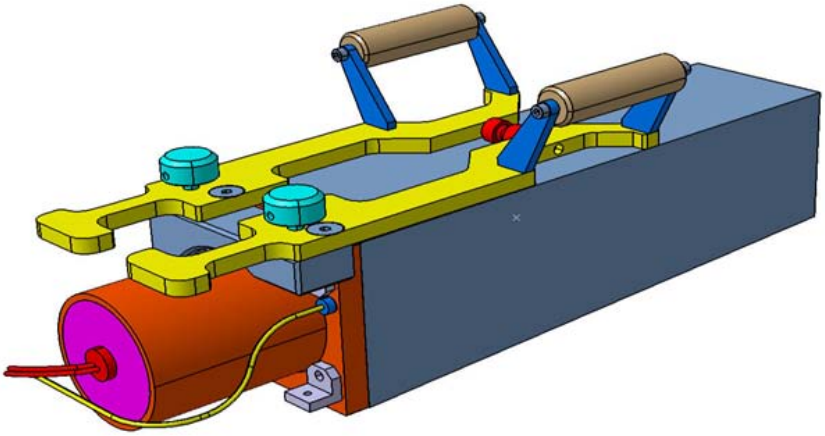

Figure 35 The lifting tool for individual blocks

Reinforcement plates are glued across the junction between the glass and the steel flange on the four crystal sides, to guarantee better mechanical resistance. The glue used is DB490 by 3M, a two-component epoxy resin. The following gluing procedure have been proved to sustain stresses as high as 40 times the crystal weight in the vertical direction. The detectors are positioned inside the holes of a 4.0-m long gluing workbench (Figure 36). They are oriented vertically and a specially designed gluing rig is placed on the top and left in position for five hours for glue curing.

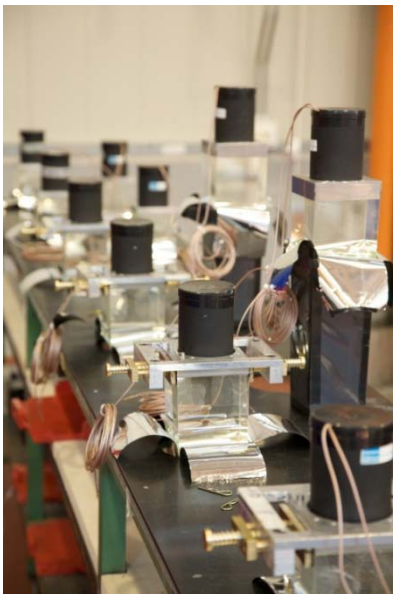

Figure 36 The gluing workbench

After reinforcement, the detectors are wrapped to increase light collection. Wrapping is not required to be light-tight, since detectors will work in complete darkness. The wrapping material consists of laser-precut sheets of DuPont 4173D-Tyvek, chosen because of its high load resistance: with a weight of 75g/cm^2 and a thickness of 205 μm, it can sustain up to 60 N/m^2. The Tyvek is folded over a block mock-up and the folded ends soldered together to give it the correct shape. The formed wrapping has holes to be anchored by screws to the holes on the flange at the top (Figure 37).

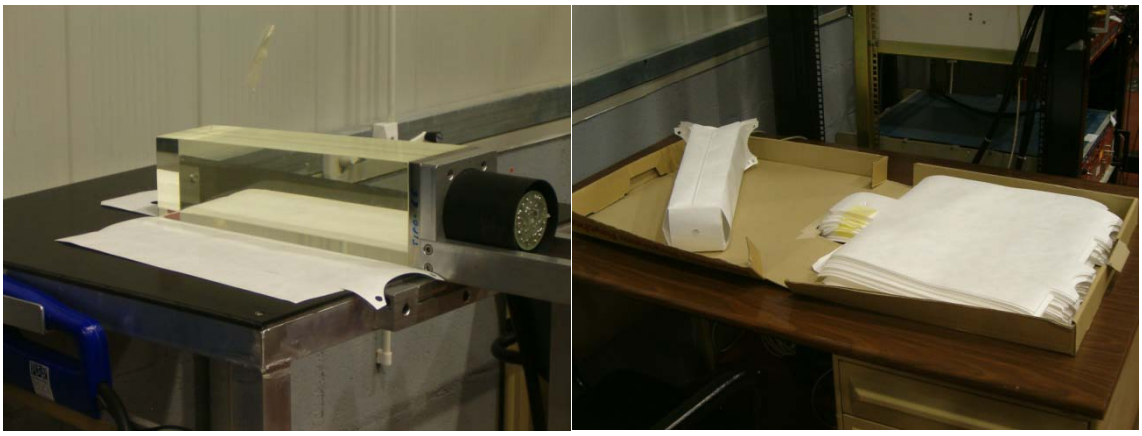

Figure 37 Wrapping preparation

The detectors are gripped by attaching the lifting tools to the aluminum mounting hardware and are then taken to the test area. Here tests of electronics, continuity, etc. are performed continually during the installation period.

In groups of four, the detectors are then mounted in the support brackets, mainly made by two aluminum plates connected to each other by cylindrical and square spacers (Figure 17). The plates have two circular and one square holes per side, guaranteeing access for tightening the support screws to the vessel and for mounting a suitable lifting tool. Crystals are connected to an azimuth segment by stainless steel screws. For each lead glass block the high voltage, the signal cable and optical fiber are routed and fixed into the mechanical structure. At the end of the operation the fibers are checked for light transmission using a LED. A completed segment with four crystals is shown in Figure 38. The assembly is then moved using a cart and a special lifting tool (Figure 39) which uses the central hole of the support structure for the connection and has a plate underneath the crystals as a protection in case of damage during handling.

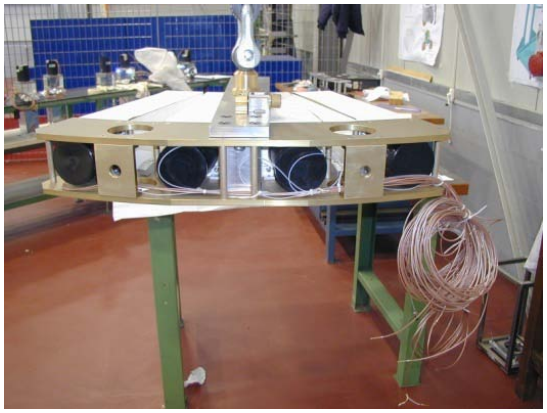

Figure 38 A complete azimuth segment with four crystals.

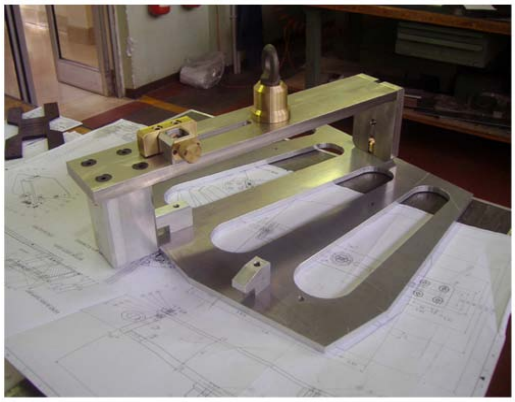

Figure 39 The special handling tool for assembly structures

Since the entire detector structure must operate in vacuum, all the screws used in the mounting and installation either are traversed by an axial hole or they are milled on the side to avoid virtual leaks during pumping; moreover all the screws and the support structure components are cleaned in an ultrasound bath.

1.1.3.9.3 Installation of the blocks into the cylinder

During the installation the cylinder is placed with its axis in the vertical direction (Figure 40), on three concrete blocks with reinforcement frame, the cable mounting grid is installed (

Figure 41) and a first protection ring is lowered into the cylinder, for the safety of the personnel working inside the cylinder in the event of a mechanical failure (Figure 42).

Figure 40 Installation of the vessel for mounting.

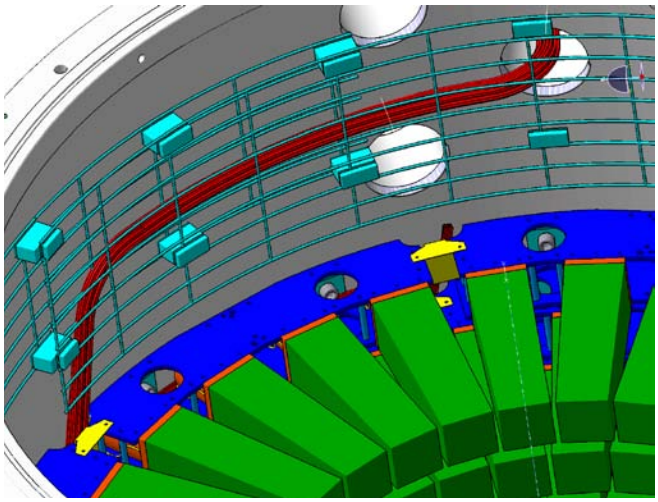

Figure 41 Detail of the cable grid.

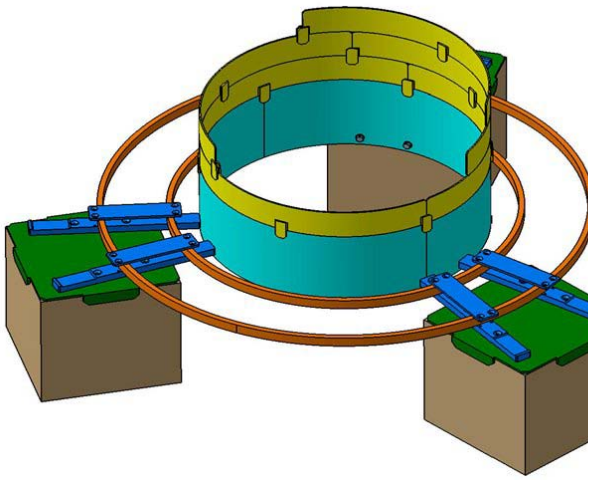

Figure 42 The protection structure.

One azimuth segment, with the lifting bar and safety plate attached, is lowered into the cylinder. The crane movements are performed by an operator on an elevated stand with an unobstructed view of the operation field. The operator lowers the detector segment into the cylinder from above, while the operator inside the cylinder anchors the piece to the cylinder wall and removes the lifting bar (Figure 43). Immediately afterwards, the cables are fixed to the grid and routed towards the portholes for cable exit. This operation is carried out repeatedly during the assembly phase.

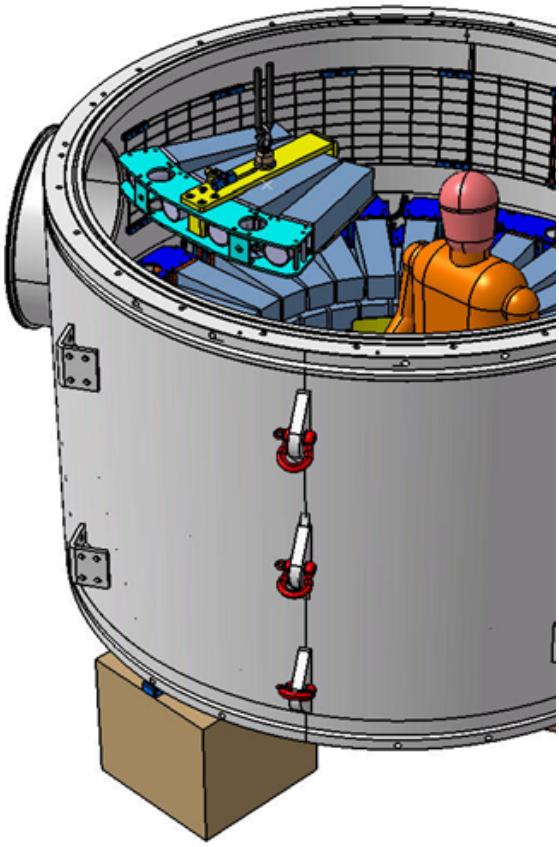

Figure 43 Mounting of a crystals.

One day is needed to mount and cable one layer of crystals. Before mounting the subsequent layer, the cosmic ray signal of each lead glass at a voltage of 1.2 KV is checked using an oscilloscope.

The previous operations are repeated for each layer; once the mounting and cabling is completed, additional checks of the signal and of the optical cabling are performed using the final HV, signal and optical fiber feed-through connections. The final module is shown in Figure 44.

Figure 44 Inside view of one completed LAV module.

1.1.3.9.4 Rotation, Electronics and vacuum testing

To prepare for the vacuum test, the cylinder is rotated by means of an appropriate tool (Figure 45) and it is placed on its feet in the horizontal position and leveled by adjusting the leveling screws. The O-rings are lubricated with vacuum grease and seated in the flanges at both ends of the cylinder. The two yellow cover flanges are lifted and mounted on the flanges of the cylinder. The 24+24 class 8.8 M20 bolts on the two flanges are then tightened to a torque of 250 N m. A 100-mm port on the manhole allows the installation of a vacuum valve and a turbomolecular pump. A disk with reduced aperture of known conductance is installed inside for the measurement of the outgassing rate.

Figure 45 The rotation stand

The pumping system consists of a scroll pump for the roughing stage, of a turbomolecular pump installed on one of the endcap flanges, and of another turbomolecular pump installed on the manhole flange for outgassing measurements (Figure 46 and Figure 47).

Figure 46 Pumping connections - Small flange side.

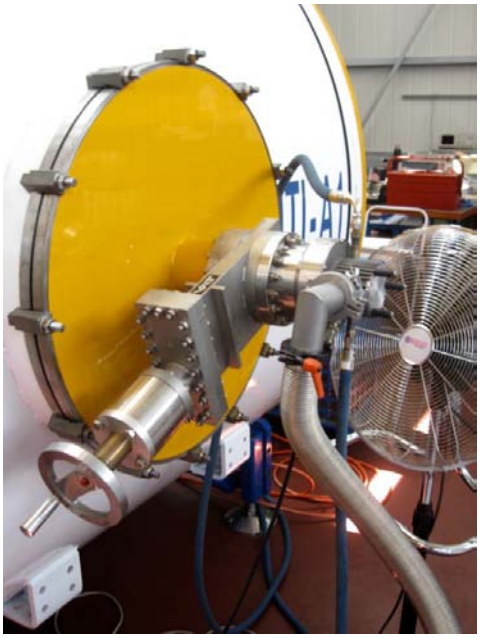

Figure 47 Pumping connections - Manhole side.

After the vacuum test is completed, one of the turbomolecular pumps is left on for several days to allow measurement of the specific outgassing rate (see 1.1.3.4.2).

At the pressure of 10^{-5} mbar, a voltage of 1200 V is applied to all photomultipliers and an additional check of the signals is performed.

1.1.3.10 Transport Procedure

The completed stations are to be shipped approximately 940 km from Frascati to the CERN Prévessin site. The first LAV station was shipped from Frascati at 18:30 on 21 July 2009 and arrived at the Prévessin site the next morning at 09:00. The load included, in addition to the first LAV station, the equipment needed for its rotation and handling, for a total weight in excess of 15 tons. The speed of the transport vehicle, a canopy truck, was limited to 90 km/h. Two technicians involved with the logistical planning followed the vehicle. The transport went smoothly, so that we can extrapolate from this experience with confidence. The primary concerns in planning for the shipping were to minimize the exposure of the station to thermal stresses and mechanical shocks.

To minimize thermal stresses, the station was transported during the night. It was not possible to load and unload the station from a thermostatically controlled vehicle. While canopied truckbeds provide easy overhead crane access, loading and unloading from a vehicle with insulated walls would have required a 10-ton forklift, which was not readily available. The construction of a thermostatically controlled shipping container was likewise judged to be unwarranted. Shipping of the module at night eliminated the problem of excessive heating in the summer sun and optimized travel time during which the module was in an uncontrolled environment. There are legal restrictions on the number of hours a single truck driver may operate a vehicle without a suitable resting period. Given the 90 km/h speed limit for the transport, two drivers are needed if the transport is to be completed without stopping for a substantial rest period during the day.

Once on the truckbed, the station was draped with quilts of fiberglass insulation heat sealed between sheets of Propacktene polyester/aluminum laminate. The station was also fitted with two max/min glass-bulb thermometers, as well as with two continuously recording temperature sensors in the shock recorders (see below). Analysis of the recorded data showed that the maximum temperature of 30 ^{0}C corresponded to the temperature of the assembly hall at departure, and that the minimum temperature of 25 ^{0}C was reached during the early morning hours and remained stable until arrival. These results demonstrate the adequacy of the measures taken to prevent excessive thermal stress for summertime transportation. Since heating of the station in direct sunlight is considered to be the primary thermal risk, summertime transport is expected to be more challenging than wintertime transport.

The following measures were taken against mechanical shock:

- The module was transported on end, i.e., with the axis of the crystals in the horizontal plane. This configuration was thought to be the most stable one; in addition, the stress on all crystals due to vibrational shock in the vertical direction is the same.
- Open-cell polyurethane foam wedges were tightly fitted in the horizontal planes between the crystals on different layers. The modules on the bottom layer were supported on foam blocks. An aluminum cylinder slightly smaller than the inner diameter defined by the crystals was placed on the central axis of the station to hold the foam wedges and blocks in place.
- When loaded onto the truckbed, the station was placed on a Sylomer R (Angst+Pfister) closed-

cell polyurethane foam mattress about 20 cm thick. The mattress was designed to reduce the vertical acceleration at 25 Hz (the fundamental resonance frequency of the crystals) by a factor of 20.

- The 90-km/h limit on the speed of the truck reduced the intensity of vibrations and shocks to the station.
- The shock absorbers of the trailer contributed some protection against major vertical shocks. The LAV station was positioned on the truckbed at the point where vibration damping by the suspension was most effective.

Two ShockLog RD298 shock recorders were rigidly fixed to the hull of the vessel for transportation. The acceleration threshold at which the recorders started to register detailed event data was set to 1 g on each of the three axes. No events were recorded on either of the transverse axes; accelerations in the transverse direction remained below the level of 0.2 g. There were two events in which the vertical acceleration was greater than 1 g and thus recorded in detail. In these events, the acceleration oscillates sinusoidally with a frequency just under 1 Hz. The largest momentary acceleration reached was 1.5 g, well within the alarm threshold of 3 g.

1.1.3.10.1 Installation Procedure

All the modules, except the LAV 12, are connected to the vacuum of the main decay tank (blue tubes). The vacuum should be around 10^{-6} mbar and it is important that the flanges are flat and well aligned to provide good tightness. The gaskets providing the seal for the vacuum are "O-Ring" type "Viton" material with hardness of 75 shores and 7mm core diameter. The flanges will be tightened with 24 M20 x 90mm screws in high-tensile steel, type 10.9, with 90kg/mm^2 of tensile resistance.

The installation sequence will be mostly identical for 11 modules. The last module (LAV 12) will be an exception as is not connected to the vacuum tank.

Preliminary operations:

- The module arrives, closed up with cover flanges, in the horizontal position to building 911 at CERN. Here it is unloaded and lowered with the overhead crane (40T) to the ECN3 pit where it is then transported by trolley to the TCC8 area.
- In the TCC8 area the module must be rotated to the vertical position using the same custom made rotation tool used during the mounting phase (Figure 48) . At the same time it is equipped with its four feet for support and adjustment.

Figure 48 Performing module rotation at CERN

Figure 49 Vacuum test before the installation

- Following the rotation, one flange is opened to inspect the inside and to remove the transport protection from the crystals . If no damage is found, the cover flange is mounted again and the module can be dressed with all the components needed for a vacuum test (Figure 49).
- After the vacuum test the two cover flanges are removed and the module is prepared for connection to the decay vessel.
- At the same time the circularity and the planarity of the two flanges of the blue tubes are measured, upstream and downstream of the module. If the divergence, particularly of the circularity, is more than 3 mm then a special tool will be used to restore the circularity inside the prescribed tolerance.

Installation phase:

All LAV modules (except LAV12) are connected to the vacuum vessel (Figure 50) with a fixed flange connection on one side and the sliding ring connection on the other (Figure 51).

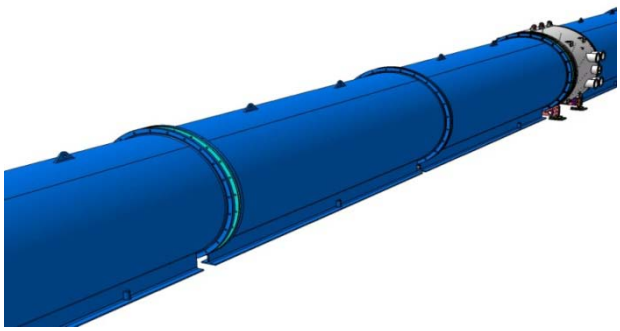

Figure 50 Module between the blue tubes

The connection with a sliding ring allows, in case of necessity, to remove the modules from the decay tank without dismounting other tank elements.

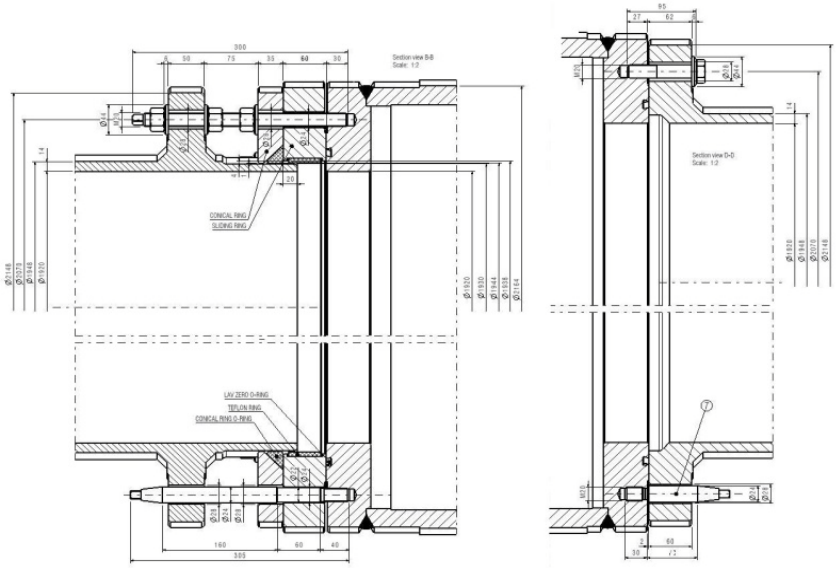

Figure 51 Left: Sliding ring connection – Right: Fixed flange connection

First stage:

It is advisable to check the circular shape and the planarity of the two connecting flanges from the vacuum tank before connecting the LAV module (Figure 52). If the variations of the vacuum flange diameter exceed 2.5mm a special tool is used to restore the circularity of the flange.

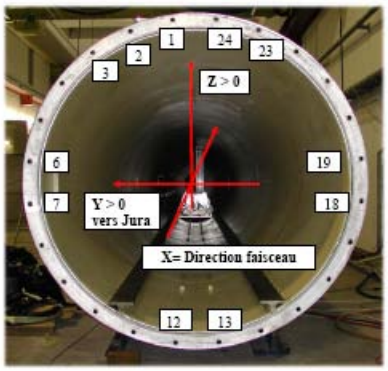

Figure 52 Survey of the blue tube flanges

Second stage:

The LAV module is brought in position using the overhead crane, the fine positioning is made using adjustable ropes (Figure 53). The connection to the vacuum tank starts on the side with the fixed flange where two conical rods, fixed on the module, guide the module to the contact with the flange. At this point 24 M20 bolts are inserted and the flanges are tightened.

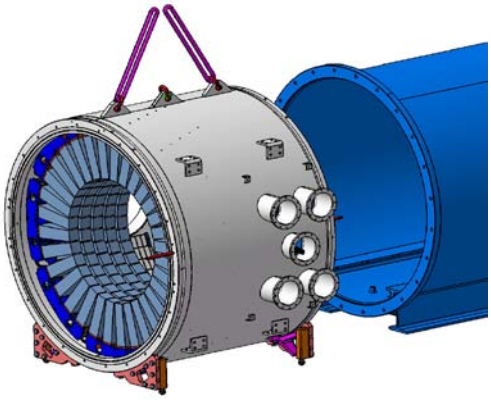

Figure 53 Module hanging from the crane

Third stage:
After checking the axis alignment the four adjustment screws in the feet are lowered and the module is disconnected from the overhead crane (Figure 54).

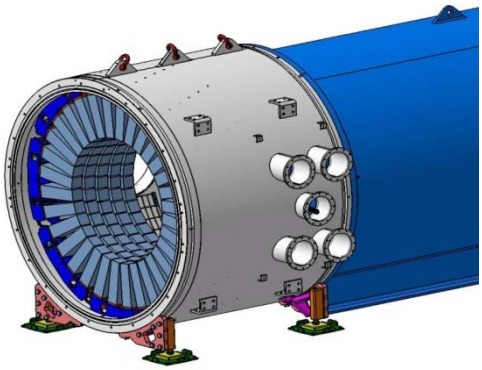

Figure 54 Module in final position

Fourth stage:
The sliding ring is placed on the two long conical rods on the opposite side of the module (Figure 55).

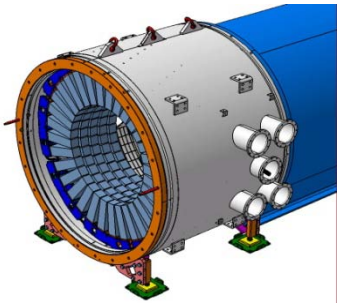

Figure 55 Sliding ring pre assembled

The overhead crane is used to bring the vacuum tank element in front of the LAV module. The two conical rods serve again to guide the vacuum tank onto the flange of the LAV module (Figure 56).

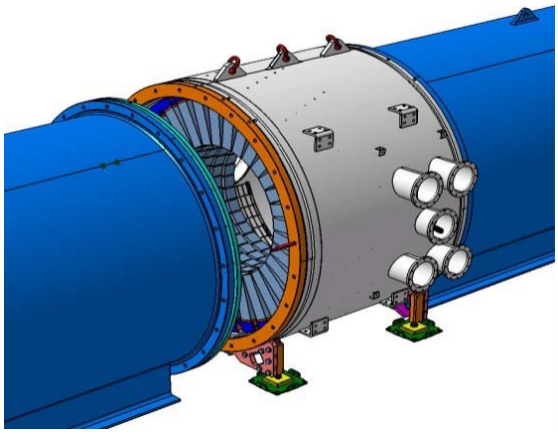

Figure 56 Approach of the blue tube to the module

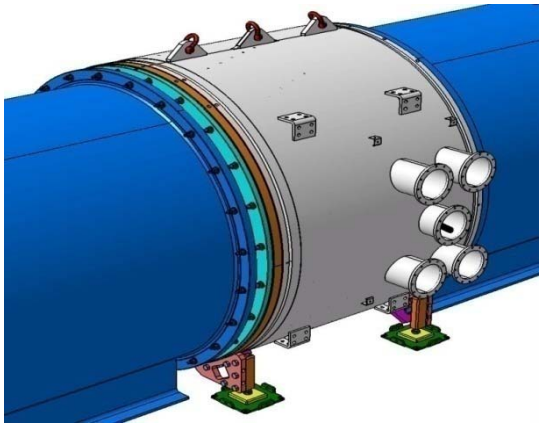

Figure 57 Module installed on the decay channel

After the connection to the LAV module the opposite flange of the vacuum tank element can be aligned to the beam axis. (Figure 57) shows an estimate of the time needed for the installation of one LAV module.

Table 9 Installation time estimate for one LAV module

Operation	Time (h)
Module arrives to building 911, unloaded and lowered by crane to the pit ECN3, transported by trolley to TCC8	4
Module rotation	2
Dismount flanges, remove inner protection, re-assemble flanges for the vacuum test.	3
Vacuum test	48
Dismount flanges, installation on the channel, insertion and tightening of the 24 screws.	4
Survey and align the module	4
Preassemble sliding ring	1
Installation of the blue tube	4
Total	74

1.1.4 The Liquid Krypton Calorimeter (LKR)

1.1.4.1 Calorimeter Requirements

As it has been explained in section 1.1.1, the Liquid Krypton Calorimeter is a key element for vetoing photons from K decays, with the requirement to have a photon detection inefficiency of better than 10^{-5} for energies larger than 35 GeV. In addition the calorimeter is supposed to provide trigger signals based on energy deposition to contribute reducing the L0 trigger rate.

Figure 58 The LKR calorimeter during the dismantling of the NA48 experiment.

Another important requirement imposed to the readout is the capability of reading interesting events with a basic hardware zero suppression (or even without), leaving to offline algorithms the optimization of this job: for example, disentangling a photon shower from a nearby charged pion shower could be tricky if a unique hardware zero suppression algorithm is implemented.

The performance of the calorimeter as used in NA48 has been checked to be good for NA62. Since the L0 rate is expected to be two order of magnitude larger, the old readout system will no longer be usable, as it was limited to 10 KHz (and many of its components are obsolete already).

In addition, other subsystems (e.g. the calibration system logic and software) will need updating. The calorimeter is fully described in (7), and because of that, it will not be described in detail here.

1.1.4.2 The new Readout of the Calorimeter

The readout system of the calorimeter should be updated. Indeed the old CPD-based system has a pipeline memory which can keep the data for 200 μs and the readout of the 64 channels in each individual CPD modules is done serially, limiting the readout rate to 10 KHz. The expected rate of L0 triggers in NA62 is of the order of 1 MHz and the latency of the L1 is of several seconds. This will rule out the use of the CPD pipeline memory. The idea is then (see a complete description in section **Error! Reference source not found.** on page number **Error! Bookmark not defined.** to have FADCs feeding a circular buffer with a depth of few seconds, a logic to allow events flagged by L0 to be transferred to a linear buffer of a suitable dimension and a readout procedure which will send L1-selected events to event building PCs using Ethernet. The new system will use commercial-of-the-shelf (COTS) components such as standard DDR2 memories, Gigabit Ethernet (GbE), network switches and standard PCs (processor nodes).

The system will also provide sums of the input signals to the trigger system.

1.1.4.3 The Calibration System

The calibration system is used both to monitor and calibrate the cell response and to spot possible problems in the readout chain. Calibration data are taken in the so-called “out of burst” period, namely 0.5 s, in order to not upset the neutral trigger response during the burst.

The calibration system hardware consists of:

- A calibration pulse generator, which produces signals to the calibration pulser and which has some programmable characteristics, like in-burst (if needed)/out-burst frequency, synchronism with the clock frequency, delay w.r.t. the clock system, etc
- A set of 30 pulser boards which receive the above pulses and which can be programmed to pulse any combination of their 8 outputs
- A 16-bit DAC which provides a voltage reference for the calibrators
- A multiplexer which distributes the DAC voltage to 8 channels connected to specific calibration patterns

It is planned to have a complete renovation of the calibration system, including an upgrade of the logic used to generate the pulses and control the system, moving from old NIM and CAMAC modules to a simple programmable VME system.

1.1.4.4 The Neutral Hodoscope

The neutral hodoscope is a detector made up of scintillating fibers which is installed inside the calorimeter at the depth where the shower development is at its maximum (6). The photomultiplier

gain has been once equalized and the HV channels are grouped in two HV connectors on the outside HV flanges.

Signal cables are going from one of the brass boxes on top of the calorimeter to the Technical Gallery. The original cabling and amplifier connections has been left in place and it will be relocated in due time.

In case of use, the neutral hodoscope readout should be a new one, because, for past experiments, it was read by the old PMB system (now dismantled). It needs anyway an amplifier system. The readout could be done for example either by the LAV or by the RICH electronics.

1.1.4.5 The Cryogenic System

The complex cryogenics system of the calorimeter has been working for more than twelve years to maintain the calorimeter in a fully operational state at the temperature of the liquid krypton. An upgrade of the control system has been done recently. In order preserve the cold parts of the calorimeter in optimal conditions the collaboration has decided not to empty the calorimeter during the installation period. The main issue here is that repeated temperature cycles may increase the failure probability of the cold electronics (preamplifiers) inside the calorimeter.

However, a list of items that need consolidation on the cryogenic system has been established, and it is considered that the repair work can be carried out while keeping the liquid Krypton inside the calorimeter.

The following main interventions have been planned:

- Replacement of the pump of the Ar cooler vacuum system and its integration in the control system
- Repair of a blocked valve on the Liq. N2 line of the emergency cooler
- Control and replacement of leaky HV feed-troughs
- Adding another pump on the Monotube[1] vacuum system as a backup and its integration in the control system
- Cleaning of the Monotube
- Replacement or improvement of the vacuum valves on the Monotube (Guillotine Valves)
- Various maintenance operations (like change of the thermal insulation)

Moreover, dissemination of the information about the operation of the cryogenics system is under way, as the people with experience of the system are retiring and new people will follow the operations. A formal agreement with the CERN cryogenics support group for the sharing of responsibility is under preparation.

[1] The term Monotube refers to the aluminum beam pipe inside the calorimeter.

1.1.5 The Small Angle Vetoes (SAV)

1.1.5.1 General requirements

In order to provide hermeticity for photons flying at angles approaching zero with respect to the kaon flight direction, two photon veto detectors are necessary. One of them, the inner ring calorimeter (IRC), is to be placed in front of the LKR, and the other, the small angle calorimeter (SAC), at the end of the experimental setup. The spectrum for photons from $K^+ \to \pi^+\pi^0$ decays in the fiducial region for $K^+ \to \pi^+ \nu\ \nu$ decay is shown in Figure 59. Cuts on the kaon decay vertex, on the pion momentum (15-35 GeV) and on the LKr acceptance have been applied. The total energy spectrum is different from that one due to additional contribution of kaon decays further downstream and muon halo of the beam.

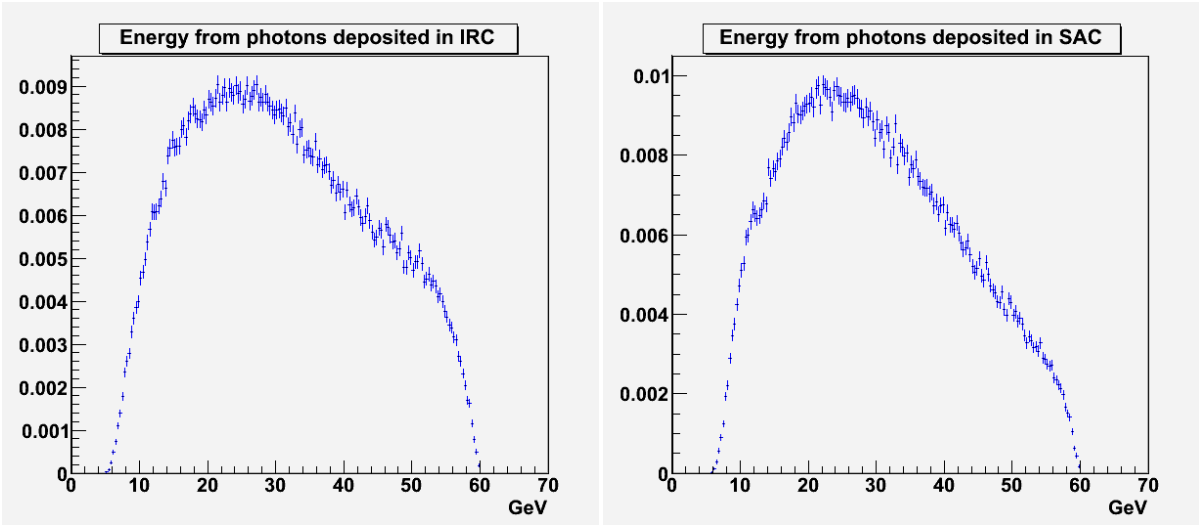

Figure 59 Photon energy in the IRC and in the SAC

Both the SAC and the IRC are exposed to photons with energies higher than 5 GeV. In order to achieve the necessary suppression of the background from $K^+ \to \pi^+\pi^0$ decays, both the SAC and the IRC have to provide detection inefficiency better than 10^{-4}.

The IRC detector will be situated around the beam pipe and its active volume should start as close as possible around the non-decayed kaon beam, and yet far enough away so that the beam halo doesn't generate extremely high rates. The SAC is at the end of the experiment with the only geometrical requirement to cover the region not covered by the IRC and LKR, and to have dimensions small enough not to interact with the deflected non-decayed beam.

The SAC and the IRC are exposed both to kaon decay products as well as the muon halo of the beam. The expected rates are few hundreds of kilohertz during the burst time for photons from $K^+ \to \pi^+\pi^0$ decay. These photons form almost the total rate in SAC while the majority of the events in the IRC will be from the muon halo (rate of 6 MHz). Since the SAC and the IRC are basically a single channel detector, the readout electronics should be able to sustain such rates and to provide good time resolution in order to have a low probability for random coincidences with the events of interest.

1.1.5.2 Description of the Shashlyk Technology

A detector of “shashlyk” type is based on consecutive lead and plastic scintillator plates. The first such detector was suggested in 1991 by Atoyan et al. as an electromagnetic calorimeter for the E-865 BNL experiment devoted to the search for lepton flavour violating decay $K^+ \rightarrow \pi^+\mu^+e^-$ (8). The incoming electron or photon interacts with the lead and develops an electromagnetic shower. The charged products of the shower produce scintillation light inside the plastic material which then could be absorbed and re-emitted to longer wavelengths by fluorescenting additions. At these longer wavelengths, the attenuation length of the plastic is lengthened considerably. The light is taken out by wavelengths shifting fibres (WLS) where a second wavelength shifting takes place usually to the green part of the spectrum to a photodetector (most commonly photomultiplier). The fibres pass through the plastic scintillator and lead plates via holes in the plates. A schematic view of the layout is shown in Figure 60.

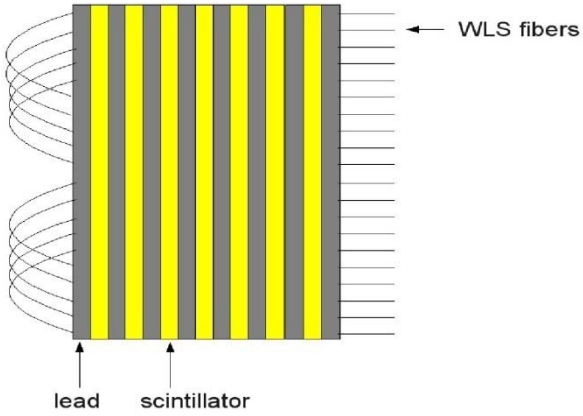

Figure 60 Shashlyk technology

The choice of lead for radiator and photon converter is motivated by the fact that lead has the maximal radiation to interaction length ratio. For a full general description of this type of calorimeter see (9).

A single module of shashlyk type calorimeter is also a single channel detector. The attenuation length of the emitted scintillation light in the plastic scintillator is much longer than the actual transverse size of the module which leads to light in all the fibres. It is important to note that splitting of the total number of fibres into bunches to be readout by different photodetectors doesn't diminish the single channel rate but only matches the geometry and the surface of the active photocathode area to the total surface of WLS fibres.

The shashlyk module has an internal particle detection inefficiency connected with the presence of the holes for the WLS fibres. Concerning the present application of such detectors this inefficiency is not an issue since if can be recovered by tilting or rotating the single shashlyk module as will be discussed in Section 1.1.5.5 for the SAC and section 1.1.5.6.1 for the IRC.

1.1.5.3 Results from the Prototype Tests

A Small Angle Calorimeter (or SAC) prototype was constructed and tested during a 2006 test run. The active part of the constructed prototype was assembled from 70 lead plates with thickness of 1.5mm

with 1.5mm scintillator plates in between, for a total of 21cm (~17 radiation lengths) in order to keep the punch through probability below 10^{-5}. The transversal dimensions were 20.5x20.5 cm^2. The light was taken out with 480 wave-length shifting fibers 1 mm Y-11(250)MSJ (Kuraray) which are separated into four bunches (four channels). The pitch between the holes is 9.5 mm. The assembly was done as follows: first the lead and the scintillator plates were put together to form a sandwich construction supported by four rods at the four edges of the plates. Each scintillator was wrapped in a layer of white paper. When half of the construction was assembled the WLS fibres were guided through the holes of the plates. This way of constructing the detector requires high precision of the holes coordinates with respect to the plates dimensions and with respect to the four guiding holes for the support rods. The WLS fibres were curved at the front so that both ends were readout. The rest of the lead, paper sheet and scintillator plates were put in groups of 5 layers and the WLS were guided through them in steps. When the active part of the detector was ready the WLS fibres were divided into bunches to ease their passage through the PMT supporting aluminium plate.

The detector was equipped with four conventional FEU-84 photomultipliers. The complete detector was placed inside a black-painted metal box hermetic for external light. The assembled prototype just before being closed is shown in Figure 61.

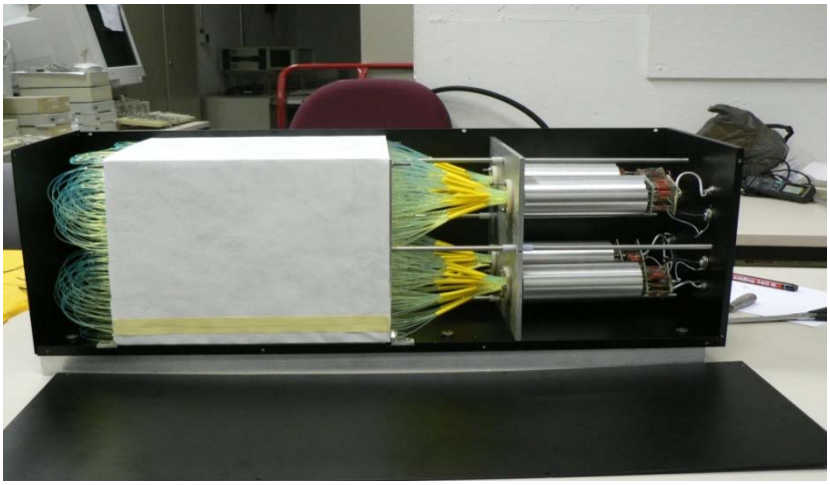

Figure 61 The SAC prototype, with the active part wrapped with white paper

The complete detector was first tested at the assembly room before being installed at the NA48 setup. Its response to cosmic muons was checked. All the channels were verified to provide signal and the time width of the signal was measured. It is a limitation factor for the maximal rate the detector could sustain. The pulse shape is shown Figure 62. Approximately 30ns FWHM was obtained. The detector was tested in 2006 with 25 GeV electron beam, using partially the setup of the NA48 experiment. The charged hodoscope was used for triggering and the magnetic spectrometer to measure the coordinates of the electrons at the SAC prototype position.

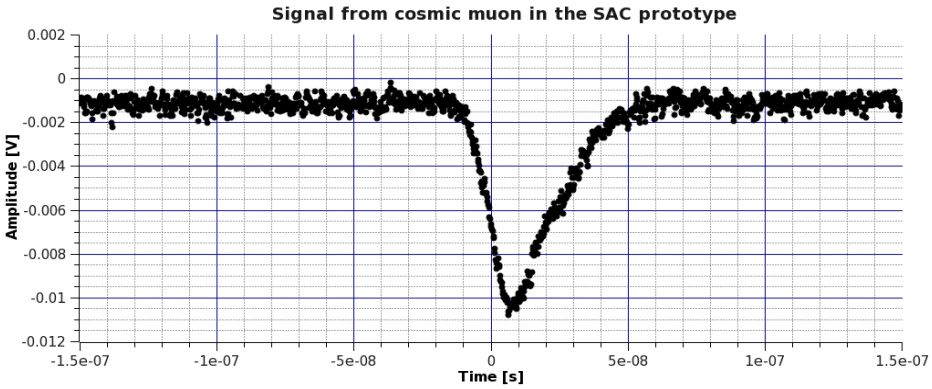

Figure 62 Oscilloscope signal from one of the PMTs of the SAC prototype for a cosmic muon

During the tests SAC was placed between the two planes of the scintillator hodoscope of the NA48 experiment. The signals were sent to an existing CPD based (10) readout of the muon veto. The CPD is based on 10-bit, 14-bit dynamic range FADCs which digitize the amplitude of the signals every 25 ns. The 25 GeV electron beam was deflected to point directly at the SAC. Several runs were taken with the beam pointing to different spots of the detector which allows to study the inefficiency as a function of the electron entry point. A total of 10^7 events were recorded.

The following preliminary results are based on 462 bursts analysed for a total of 2410184 reconstructed events. For each of the four channels, the signal is defined as the measured amplitude minus the pedestal of the channel. The total signal from SAC is

where A_i is the amplitude in channel i , and P_i is the pedestal for channel i (i=1,2,3,4) in ADC counts. In order to determine the pedestals, only the events for which there were no associated tracks in the Drift Chambers were counted. Since for these events there is no particle, the signal in the SAC is just the pedestal. The pedestals were almost constant for a particular channel during different bursts: the fluctuations observed in the first bursts while tuning was done are less than 0.1%.

The sidemost parts of the detector are expected to be less efficient. The inner area that is effective enough should be determined, i.e. the “effective” size of the SAC. The effective size of the detector is obtained by considering the tracks, extrapolated from the Drift Chambers to the Z-coordinate of SAC (i.e. expected number of tracks), and the tracks for which there was response in the SAC (i.e. detected events). The result for the active area (Figure 63) is obtained using the ratio of these two kinds of tracks (detected/extrapolated).

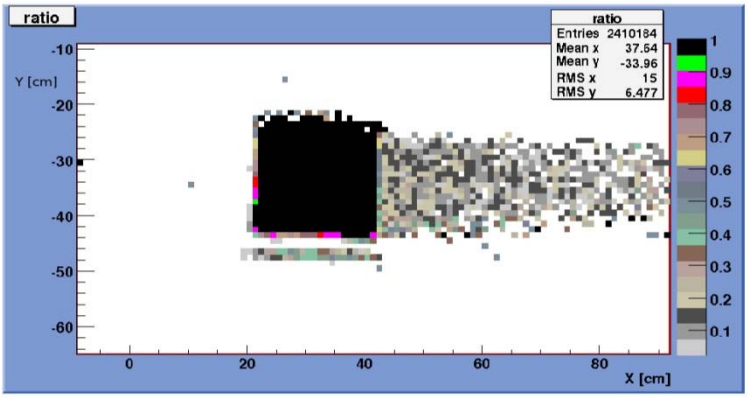

Figure 63 Measured efficiency of the SAC as a function of the photon impact point .

The effective dimensions of SAC can be considered as: X: 22÷42cm, Y: -43÷-23 cm from which the active area is 20x20 cm2. The actual coordinates of the SAC in between the two layers of the charged hodoscope were 22 < X < 43.5 cm, -44.5 < Y < -22 cm meaning that the effective size of SAC was very close to the actual physical size of the detector.

Considering the effective size of SAC, the efficiency map is studied within this area. Figure 64 shows that in general the efficiency is uniform; there are some areas that are less efficient, but the difference is approximately 10^{-4}.

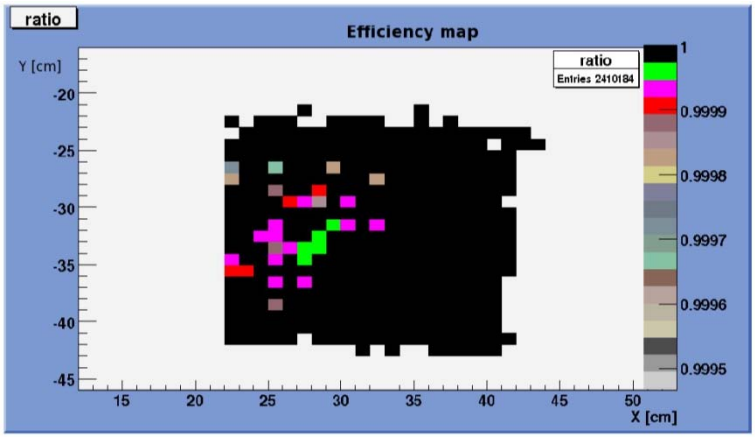

Figure 64 Map of the SAC prototype efficiency

The inefficiency for the effective size of SAC is defined as

$$\frac{\qquad\qquad}{\qquad\qquad}$$

where $N_{extrapolated}$ is the number of electrons hitting the SAC within its effective size and N_{missed} is the number of electrons that were not detected by SAC (below a chosen threshold). On the basis of the analysed amount of data the result is

This result successfully conforms to the requirements of the NA62 experiment for inefficiency less than 10^{-4}. Another characteristic of the detector is the random signals determined by the events for which there was signal in the SAC when there was no event, i.e. the track is outside of the detector and the signal in the SAC was above the chosen threshold. For this given threshold the random signals (mostly due to electronic noise) were less than 1% for the assumed event readout time window of 300 nsa nd for cut on the Drift Chambers of 25 GeV.

The Small Angle Calorimeter prototype was constructed with the financial support of the Ministry of Education and Science (Bulgaria) under contract VUF-04/05.

1.1.5.4 Materials

1.1.5.4.1 Lead plates

Since the pure lead is very soft and is difficult to work, tin enriched lead will be used for the plates production. In order to achieve the desired thickness of 1.5 mm the lead-tin alloy (96% lead and 4% tin) will be extruded. The extrusion precision on the thickness achieved for the SAC prototype was 0.15 mm per 205 x 205 mm lead plate.

1.1.5.4.2 Scintillator

The base material for the scintillation tiles is chosen to be polystyrene produced by the Amcrys-H company - the commercial branch of The Scientific and Technical Concern "Institute for Single Crystals" (Kharkov, Ukraine). Industrial granulated polystyrene will be used with PTP (para-terphenyl, 1.5% by weight) and POPOP (0.02% by weight) as dopants for the tiles production by casting technology. This type of scintillator, namely UPS-923A is developed as analogue of the BCN-400 (Bicron) and NE102 (Kuraray) scintillators. The initial excitations of the bulk polystyrene due to the passage of charged particles is transferred to the PTP (with maximal absorption at 275 nm and emission length of 340 nm) via Foersters resonant dipole-dipole interactions. The light emitted by the PTP is reabsorbed by the POPOP (abs=365 nm) and re-emitted in the blue region of wavelengths (maximal emission at 420 nm). The light yield of such scintillator is ~60% compared to anthracene and the attenuation length is about 0.5 m (depending on the coverage – aluminized mylar, tyvek). The rise time is 1 ns and the decay time of the chosen scintillator is about 3.5 ns which is enough for the expected rate of particles passing through the detector (11).

In order to provide better reflection from the scintillator surface, the plastic tiles will be wrapped in Tyvek. This will provide an increased light yield and an improvement of the uniformity of the response.

1.1.5.4.3 WLS fibers

WLS fibres are used to take the signal to the photomultiplier. The chosen type of fiber was multi-cladding Y-11(250)MSJ of KURARAY with 1.2 mm in diameter. The attenuation length inside the fibres is higher than one meter and the usual decay time of the light in the fibre is about 9 ns. The fibres are the major contributor to the length of the signal and thus to the two consequent signal separation capability of the detector. If possible an alternative fibre will be used, BCF-92 produced by BICRON, which shows the shortest decay time (about 3ns) with respect to other fibres (12). The light emitted by these fibres is with a maximum at approximately 490 nm (green light).

1.1.5.4.4 Photodetectors

Photomultipliers were chosen as photodetectors for the light from the WLS fibers. They provide gain up to 10^6. A FEU-115M-10 PMT was chosen. It has a 10 stage Al-Mg alloy linear focused dynode system. The photocathode is made from Sb-K-Na-Cs and is semitransparent. The average quantum efficiency for wavelengths in the interval 400-500 nm is higher than 12%. This PMT has been tested for LHCb ECAL and HCAL (13). The gain is between 10^3 (for 1250 V applied high voltage) up to 10^6 for 2000 V. The transit time varies from 36 to 27 ns depending again on the high voltage (1250V to 2000V). An important characteristics is the rise-time which for this PMT doesn't depend on the HV and is less than 5 ns. It also provides linearity better than 1% for anode currents up to 50mA (and even higher).

The phototube has a diameter of 30 mm with 24 mm useful photocathode diameter. The length is 72 mm and a typical base is of length 30 mm for a total of 102 mm long tube. It should be placed in a μ-metal cylinder for magnetic field shielding. The alternative phototube considered is HAMAMATSU R5800 which provides better photocathode uniformity and is operated at lower high voltage.

1.1.5.4.5 Outgassing

Since the SAC is planned to operate in vacuum the outgassing properties of the materials are important parameters. No dedicated study on the outgassing of the SAC prototype was performed. However the outgassing of scintillator, lead and Tyvek paper assembled at Protvino as a potential prototype module for the MUV has been tested. The obtained results both from the CKM collaboration during the tests of the Protvino module (14) show that the most leaking material is the scintillator. The rate was found to be $1.2*10^{-7}$ mbar.l/(s.cm^2) after five days of pumping. The total expected outgassing from the SAC was calculated assuming the total scintillator surface and was found to be approximately $6.1*10^{-3}$ mbar.l/s. Taking only into account the dimensions of the tube where the SAC will be located (rough estimate of ~50 cm diameter, ~7 m long), this turns into $1.1*10^{-6}$ mbar/s.

1.1.5.5 Mechanical Design of the Small Angle Calorimeter (SAC)

The SAC will operate in vacuum and will be placed on a rail in an approximately 7 m long 100 cm diameter vacuum tube. The schematics of the placement of the SAC in the NA62 complex is shown in Figure 65.

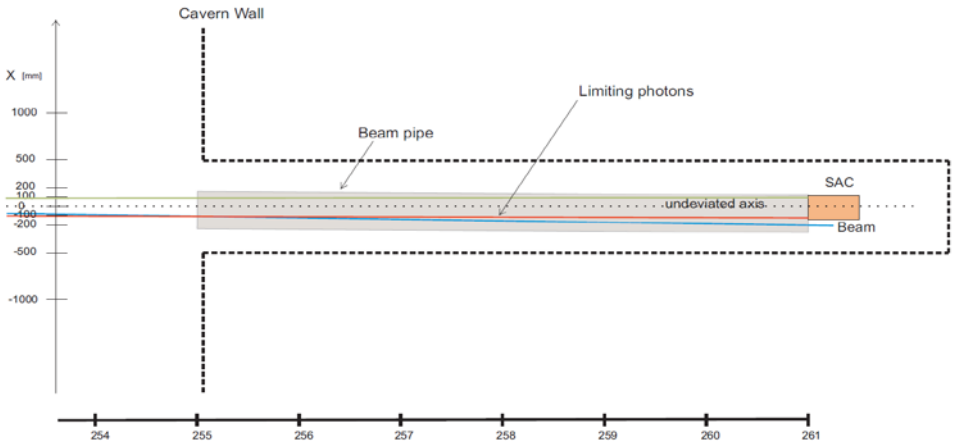

Figure 65 Placement of SAC inside a vacuum tube. The deviated beam is also shown

The detector itself will stay on a table which will be supported from below on two rails which will be welded to the inside of the vacuum tube. The table will have ability for height adjustment (Y axis) and rotation in the XZ plane (along Y axis). The detector will be put at a small angle with respect to the X axis in order to avoid the possibility of a photon originating from the fiducial region to pass completely along a scintillating fibre. The studies show that an angle of few mrads is enough to recover the high efficiency for photon registration (Figure 66). This angle can also be obtained by just requiring that a photon parallel to the non-deviated axis passes at least through part of the converter material (taking 1.5 mm the hole diameter per 210 mm active detector leads to an angle of 7 mrads).

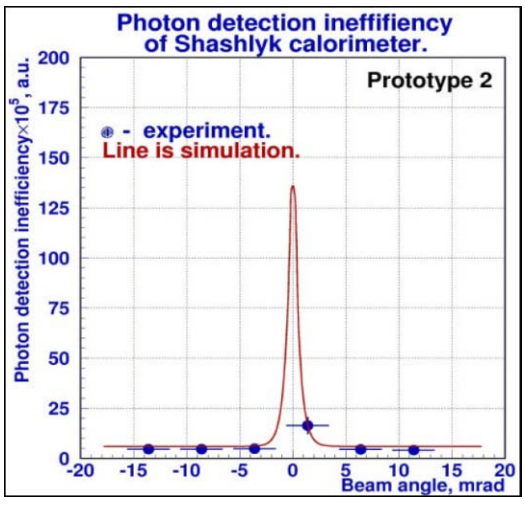

Figure 66 Shashlyk calorimeter inefficiency as a function of the beam angle (15).

The lead plates will be manufactured by the Laboratory for Technical Development in Physics, Bulgarian Academy of Science (as a subcontractor, resources from project DID02-22/17.12.2009, Ministry of Education, Youth, and Science, Bulgaria). A total amount of 80 square plates will be produced with dimensions (205 ± 1) mm times (205 ± 1) mm and thickness (1.5 ± 0.15) mm (

Figure 67). Symmetrically with respect to the center of the plates 484 holes with diameter (1.5 ± 0.05) mm will be made in 22 columns each with 22 holes. The distance between the centres of the holes in each row and between adjacent rows will be (9.5 ± 0.05) mm. The distance between the centres of the outermost holes will be 195.5 mm so leaving 1mm distance from the edge of the hole to the edge of the plate.

In the four corners of the plates 4 bigger holes will be made for the support rods – again symmetric with respect to the central axis of the plate, the centres of which form a square with dimensions 190mm x 190mm. 70 out of the 80 plates are necessary for the production of the SAC, 10 more are intended to be used in case of obstructed holes. During the prototype construction only one out of 33880 holes in the lead was blocked (probability ~$3*10^{-5}$). This could happen since during the drilling process there is a chance that the remnants of the lead fall into the hole and remain there due to high lead plasticity. As in the prototype, the SAC will be 21 cm (~17 radiation lengths) thick.

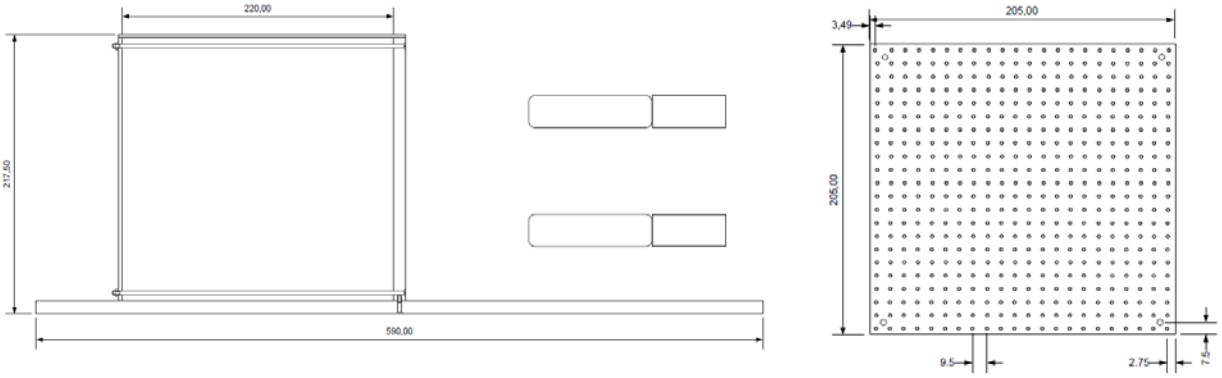

Figure 67 SAC general layout and a single lead plate

A special matrix for drilling holes in the lead will be used. The same matrix afterwards will be used to drill holes in the scintillators. The scintillating tiles will be the same size as the lead ones. The holes will have (1.4 ± 0.15) mm diameter and again the pitch between them is (9.5 ± 0.05) mm.

Tyvek paper will be put between the scintillator and lead plates. Also the whole detector will be wrapped in TYVEK. The assembly of will be done with the detector lying on its supporting main plate (shown below, also used as the table for the support on rails). Lead, paper and scintillator will be put vertically and the fibres will be strung through their holes, layer by layer. 1 meter WLS fibres read from both ends and curved at the front will be used – long enough to assure a curvature diameter of 5cm (shorter radius leads to light loss) in the front of the SAC and to operate freely when combining them at the back.

In order to support the lead and the scintillator tiles a front plate of 4mm thickness made of aluminium is foreseen. It will have the same distribution of holes like the converter plates with the only difference of the diameter which will be 3mm. The packed active SAC volume will be tightened with screws on the supporting rods at the end of the assembly, behind another aluminium supporting plate (again with 484 3mm holes). Yet another aluminium plate will be placed 10 cm after the end of the lead-scintillator sandwich where the PMTs will be mounted (Figure 68). The 10 cm are necessary in order to have enough space for WLS fibres grouping before they go the photomultipliers.

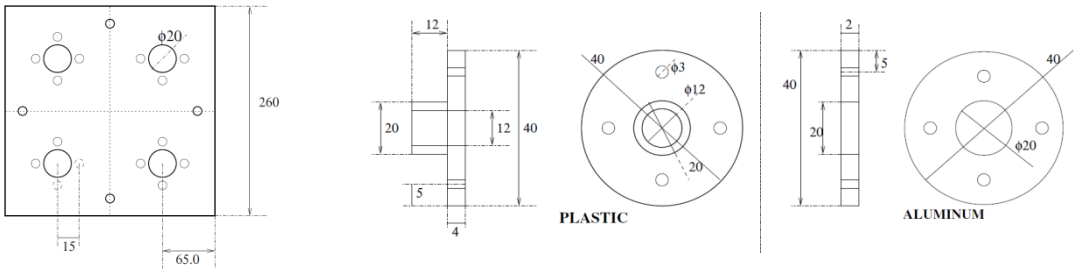

Figure 68 PMTs supporting frame at the end of the active detector volume. The WLS fibers through the hole in the plastic to the PMTs faced at them.

1.1.5.6 Mechanical Design of the Intermediate Ring Calorimeter (IRC)

1.1.5.6.1 Detector design

The detector will be made as a cylindrical tube (ring) with two active regions. The first half will be with 25 layers of lead and scintillator while the second half will have 45 layers, for a total of 70 layer sandwich. The matrix for holes drilling for both halves will be rotated at a small in order to prevent a photon from following a wavelength-shifting fibre completely through the detector, a path which would lead to a loss in detection efficiency. The outer radius of the IRC will be centred at the Z-axis of the experiment while the inner radius will be centred at the beam axis which, at the IRC coordinates, is displaced 1cm away in X-axis. In this way the detector will not have a rotational symmetry. The front half will have radius of the inner region 60 mm and an outer radius of 145 mm, while the second half will have inner and outer radii of 61 and 145 respectively.

The second half of the detector will have an inner radius very slightly larger than that of the first half in order to prevent photons hitting the detector edges too far downstream and thus escaping detection. The matrix for holes drilling will be rotated 40mrad with respect to the first half along Z axis. The small rotation angle in the XY plane of the experiment will provide the necessary coverage for the whole geometrical region.

The lead plates will be produced by the Laboratory for Technical Developments in Physics, BAS-BG. They will be made as a single ring converter. The same identical hole matrix as for the SAC with an

additional tool to fix the ring lead plate at the centre of it will be used for the holes drilling - this means a pitch between the holes of (9.5 ± 0.05) mm and a hole of (1.5 ± 0.05) mm. The distribution of the holes on the lead plate is shown in Figure 69 .

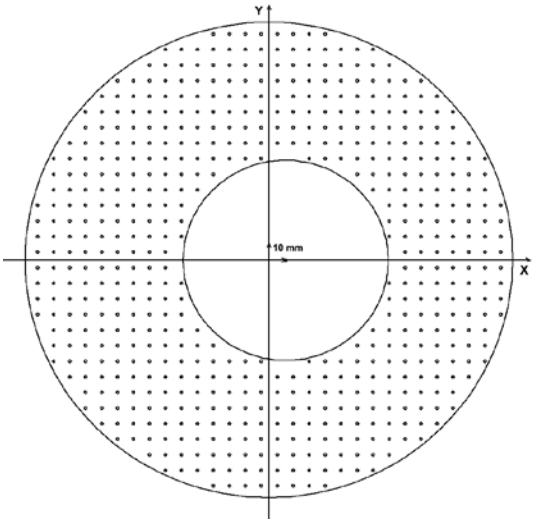

Figure 69 Layout of the holes in the IRC plates – XY plane

The high rate in the IRC could lead to event overlapping as described in the earlier sections. The width of the avalanche from electrons with 25 GeV energy in the shashlyk prototype during the tests was estimated to be about 5cm. This allows to make the inner ring calorimeter segmented into four parts, each representing 90 degrees sector (centred at the Z-axis). The segmentation will be achieved by dividing the scintillating tiles into four sectors. Each tile will have its edges aluminized in order to avoid cross talk between the four channels. The total width of the first half will be approximately 80 mm while the second will have width 140 mm (including the Tyvek, without the enclosing aluminium plates, each 5mm thick) (see Figure 70).

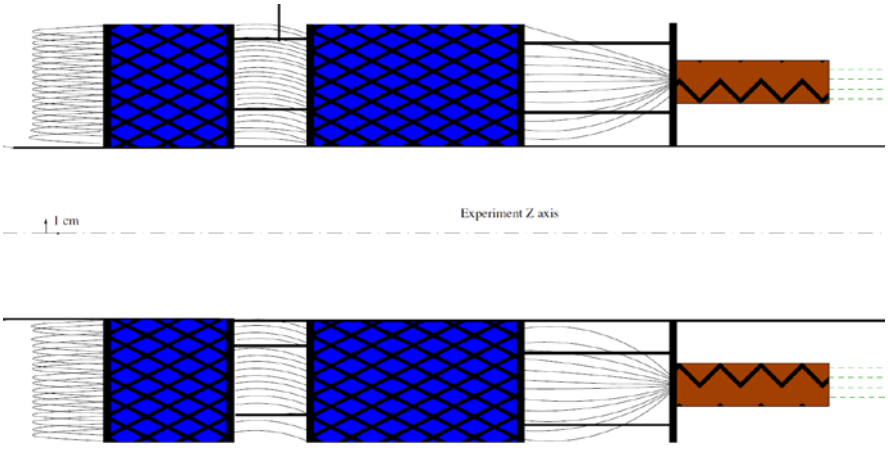

Figure 70 IRC design in the form of two halves in the YZ plane. Inner hole of the first half is ~59mm.

The IRC will be equipped with four photomultipliers with additional high voltage stabilizer in order to assure stable operation in high rate regime. The last four dynodes of each PMT will be provided with

additional high voltage supply. PMTs will be mounted on a aluminium ring located 10 cm after the closing plate of the second half of the detector. This will provide enough room for curving the fibres.

1.1.5.6.2 Support Structure and Integration

Since the IRC is a monolith detector as the lead plates are in a ring shape, it necessarily incorporates part of the beam tube. The beam tube passing through the IRC will also be made in two welded parts of 1mm stainless steel with outer diameter of 120 mm in the front and 122 mm downstream. The upstream part of the IRC beam pipe will be attached to the aluminium beam pipe passing through RICH by an elastomer O-ring made from fluorocarbon (Viton® by DuPont). It is good enough to provide small permeability for a vacuum of 10^{-4} mbar as expected in the beam tube. The downstream tube will be welded to a steel bellow which will be then connected to a CF flange, connected to the LKR guillotine valve (Figure 71).

The total IRC assembly will weight about 70 kilograms and cannot be left only on the beam pipe. The detector will hang on a string made of carbon fibre or stainless steel from a rod attached at the top of the LKR. The string will be attached to a rod located between the two halves of the IRC. The rod will be attached to the two aluminium disks enclosing the active detector region.

1.1.5.7 Readout Electronics and DAQ integration

The SAC and the IRC will use a TEL62 based readout with high-speed Flash ADC modules to be used waveform digitizers, because of the high rate. The description of the readout scheme is done in section **Error! Reference source not found.** on page **Error! Bookmark not defined.**.

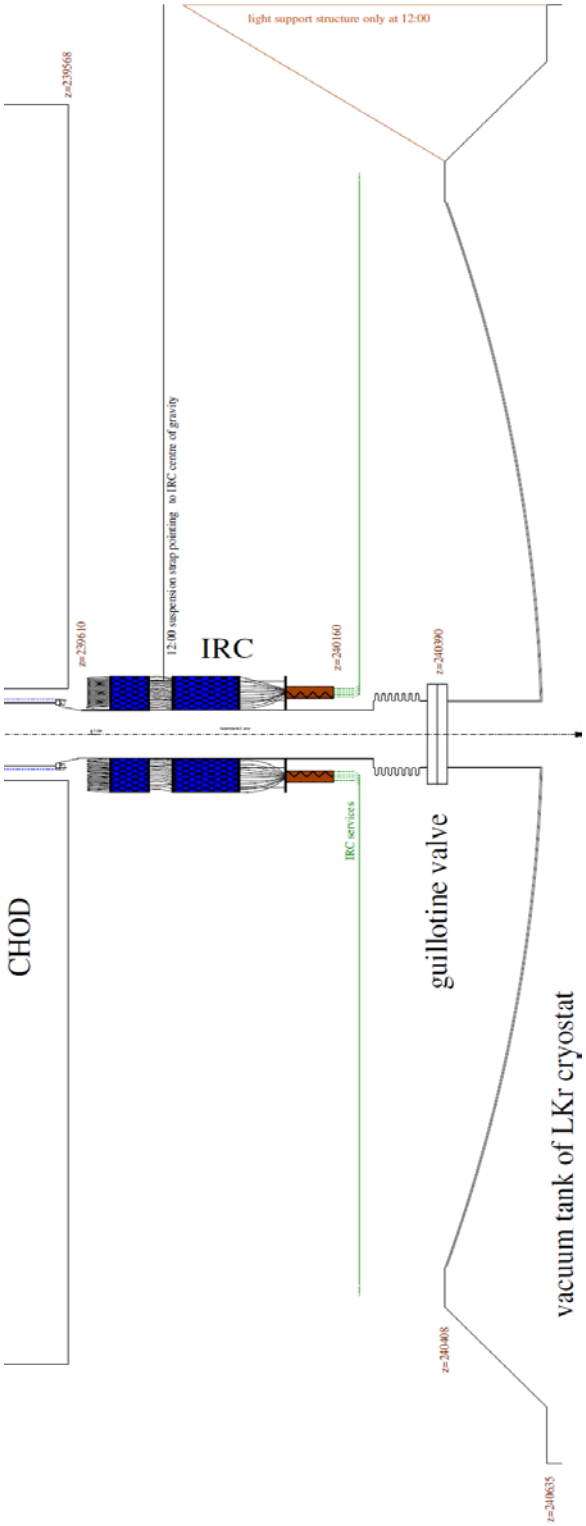

Figure 71 Integration of the IRC in the NA62 setup.

Bibliography

1. **OPAL Collaboration, K. Ahmet et al.,.** *Nucl. Instrum. Methods A, 305 (1991) 275.* 1991, Vol. 305, p. 275.

2. **F. Ambrosino et al.** Honolulu : IEEE, 2007. IEEE Nuclear Science Symposium Conf. Record. pp. N05-6. arXiv:0711.3398.

3. **Palladino, V.** Pavia : Institut of Physics Publishing, 2008. Proc. XIII Conf. On Calorimetry in High Energy Physics (CALOR 2008).

4. **NA62 Collaboration Ambrosino F. et al.** NA62 Status Report. *CERN-SPSC-2007-035.*

5. **Antonelli, A., et al.** Study of the outgassing rate of the NA62 Large Angle Photon Veto System. *Internal Note NA62-09-01.* May 2009.

6. **NA48 Collaboration; Anvar, S. et al.** The Beam and Detector for the NA48 neutral kaon CP violation experiment at CERN. *Nucl. Instrum. Methods A 574.* 2007, pp. 433-471.

7. **Fanti, V. et al.** 2007, Nucl. Instrum. Methods A,, Vol. 574, p. 433.

8. **G. Atoyan et al.** *Nucl. Instrum. Meth. A320.* 1992, pp. 144-154.

9. **G.S. Atoian et al.** *Nucl. Instrum. Meth. A531.* 2004, p. 467.

10. **B. Hallgren et al.** *Nucl. Instrum. Meth. A 419.* 1998, pp. 680-685.

11. Molded scintillators technical data. *IHEP Protvino.* [Online] 2010. http://www.ihep.su/scint/mold/product-e.htm.

12. **Brekhovskih, V. et al.** *LHCb Calorimeter Technical Note 2000-40.* 2000.

13. **Brekhovskih, V. et al.** *LHCb Calorimeter Technical Note 2000-39.* 2000.

14. **Allspach D. et al.** *CKM Vacuum Veto System Detector Outgassing Studies .* Fermilab. Chicago : s.n., March 2003. Technical Memorandum CKM-81.

15. **G.S. Atoian et al.** *Nucl. Instrum. Meth. A 584.* 2008, pp. 291-303.